

# Spin Tune Analysis for Electric Dipole Moment Searches

von  
Abhiroop Sen

## Masterarbeit in Physik

vorgelegt der  
Fakultät für Mathematik, Informatik und Naturwissenschaften  
der Rheinisch-Westfälische Technische Hochschule Aachen

im September 2020

angefertigt im  
dritten Physikalischen Institut B  
bei  
Prof. Dr. Jörg Pretz





**Erstgutachter und Betreuer**  
Prof. Dr. Jörg Pretz  
III. Physikalisches Institut B  
RWTH Aachen

**Zweitgutachter**  
Prof. Dr. Achim Stahl  
III. Physikalisches Institut B  
RWTH Aachen



## Selbstständigkeitserklärung

Ich versichere, dass ich die Arbeit selbstständig verfasst und keine anderen als die angegebenen Quellen und Hilfsmittel benutzt sowie Zitate kenntlich gemacht habe.

---

Unterschrift

---

Datum

Diese Arbeit wurde im Institut für Kernphysik (IKP-2) des Forschungszentrums Jülich durchgeführt.





# Abstract

The JEDI Collaboration aims to measure the electric dipole moment (EDM) of deuterons and protons, in order to probe physics beyond the Standard Model, and answer fundamental questions regarding the nature of the Universe, especially regarding the matter-antimatter asymmetry observed today. The first step in the search for the EDM is being conducted in the Cooler Synchrotron (COSY) in Forschungszentrum Jülich, by studying particles in storage rings. A spin polarized particle in a storage ring, subjected to electromagnetic fields along the quantization axis, will exhibit spin precession. The number of spin precessions per turn in the storage ring defines the spin tune. This measure is a vital component to the broader search for the EDM. This thesis describes the spin tune analysis procedure for data taken in the April 2019 run in COSY, which had cycles of the order of 1000 seconds.



# Contents

<b>1</b>	<b>Introduction</b>	<b>1</b>
1.1	Motivation . . . . .	1
1.2	Electric Dipole Moments (EDMs) . . . . .	2
1.3	The COoler SYnchrotron (COSY) . . . . .	3
1.4	Outline of the Thesis . . . . .	5
<b>2</b>	<b>Spin Dynamics and Polarimetry</b>	<b>6</b>
2.1	Spin and Polarization Formalism . . . . .	6
2.2	Spin Dynamics . . . . .	7
2.3	Scattering Cross Section and Polarimetry . . . . .	9
<b>3</b>	<b>Data Analysis</b>	<b>12</b>
3.1	Experimental Method and Data Acquisition . . . . .	13
3.1.1	COSY RF-Cavity Signal . . . . .	14
3.2	Discrete Turn Fourier Transform . . . . .	15
3.3	Spin Tune Measurement . . . . .	20
3.4	Uncertainty in the Spin Tune . . . . .	21
<b>4</b>	<b>Comparison Between Bunches</b>	<b>28</b>
4.1	Results from the Analysis . . . . .	29
4.2	Consistency Check . . . . .	32
<b>5</b>	<b>Summary</b>	<b>34</b>
<b>A</b>	<b>Results from Cycle 3</b>	<b>35</b>



# Chapter 1

## Introduction

### 1.1 Motivation

One of the most fundamental unanswered questions in physics currently is why the universe is made of matter and not antimatter, and what caused this imbalance to occur in the first place? According to the Big Bang hypothesis, the universe was created with equal parts of matter and antimatter which ideally should have annihilated perfectly, but due to quantum fluctuations, matter predominated and we are left with the universe as we see it today. Andrei Sakharov identified three conditions which need to be met in order to explain this asymmetry : [1]

- Processes violating baryon number  $B$  must exist
- Charge inversion (C) and charge-parity inversion (CP) symmetries must be violated
- Interactions outside the thermal equilibrium must occur.

The matter-antimatter asymmetry is quantified by the asymmetry parameter

$$\eta = \frac{n_B - n_{\bar{B}}}{n_\gamma}, \quad (1.1)$$

where  $n_B$  is the number density of baryons,  $n_{\bar{B}}$  the number density of anti-baryons, and  $n_\gamma$  the number density of the cosmic microwave background (CMB) radiation photons. According to the latest measurements of the CMB from the Planck Collaboration, the baryon density has been measured to be  $\Omega_b h^2 = 0.02230 \pm 0.00014$ , from which we get a baryon asymmetry of  $\eta \approx 10^{-10}$  [2]. Taking into account the Standard Model and known theories of baryogenesis, we expect an asymmetry of  $\eta \approx 10^{-18}$ , eight orders of magnitude lower than the observed figure. This suggests that physics beyond the Standard Model (SM) is required to explain the matter-antimatter asymmetry.

A few explanations have been posited for the baryon asymmetry, such as the

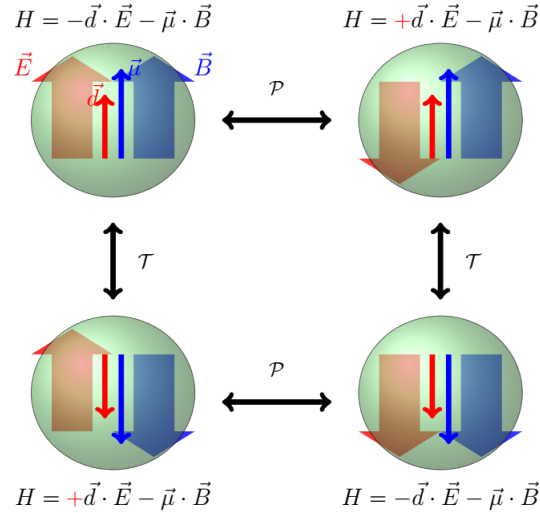


Figure 1.1: Electric and magnetic dipole moments of a particle, and their transformations under parity ( $\mathcal{P}$ ) and time reversal ( $\mathcal{T}$ ) transformations. It is seen that the hamiltonian of the system after applying both these transformations does not return to the original state, therefore violating CP symmetry. [8]

existence of electric dipole moments in fundamental particles [3], regions of the universe where the antimatter has accumulated [4], or a mirror universe which is antimatter dominated [5]. The existence of electric dipole moments would be an extremely promising area of research since they are also predicted by theories which go beyond the SM, such as supersymmetry (SUSY) or the theory of axions as dark matter particles. Each theory predicts a certain magnitude and behaviour of an electric dipole moment which can be used as a test for their validity. Axions would cause oscillating electric dipole moments in baryons [6], while SUSY predicts the orders of magnitude of electric dipole moments in fundamental particles [7]. The Jülich Electric Dipole moment Investigations (JEDI) collaboration aims to measure the permanent electric dipole moment of particles in storage rings, using the Cooler Synchrotron in Forschungszentrum Jülich.

## 1.2 Electric Dipole Moments (EDMs)

An electric dipole is formed, classically, when there is a physical separation of opposite charges in a system. The electric dipole moment (EDM) is a vector, defined as follows

$$\mathbf{d}_{EDM} = \int_V \mathbf{x} \cdot \rho(\mathbf{x}) \, d\mathbf{x}, \quad (1.2)$$

where  $\rho(\mathbf{x})$  denotes the charge density in a volume  $V$ . However, quantum field theory also predicts fundamental particles to have intrinsic EDMs which arise purely due to quantum mechanical effects. EDMs of fundamental particles  $\mathbf{d}$  are collinear with their magnetic dipole moments  $\boldsymbol{\mu}$  (MDM) and are defined as follows

$$\begin{aligned}\mathbf{d} &= \eta_{EDM} \frac{q}{2mc} \mathbf{S}, \\ \boldsymbol{\mu} &= g \frac{q}{2m} \mathbf{S},\end{aligned}\tag{1.3}$$

where  $m$  and  $q$  denote the mass and charge of the particle, respectively. The speed of light is denoted by  $c$ ,  $\mathbf{S}$  is the spin vector, and the  $g$ -factor  $g$  and scaling factor  $\eta_{EDM}$  are dimensionless. EDMs violate charge and time symmetry, which implies under the CPT theorem that they must also violate CP symmetry (Fig. 1.1). One of the consequences of a permanent EDM violating CP symmetry would be different decay rates for matter and antimatter, providing an opportunity to study the baryon asymmetry in the universe.

The Standard Model has two sources of CP violation: in the complex phase of the Cabibbo-Kobayashi-Maskawa (CKM) matrix, which describes the mixing of quark states and due to which we have observed CP violation in kaon and B meson decays [9][10], and the  $\theta_{QCD}$  coefficient of the unobserved CP violating term of the QCD Lagrangian [11]. The magnitudes of the EDMs of Standard Model particles predicted by the theory are extremely small and out of the limits of current experiments,  $\mathcal{O}(10^{-36})e.cm$  [12]. Several theories which go beyond the Standard Model predict different EDMs for particles and thus provide a test for them, such as Supersymmetry (SUSY) which predict EDMs of the order of  $10^{-28} - 10^{-25}e.cm$ . EDMs of hadronic systems are sensitive to  $\theta_{QCD}$  and other CP violating sources beyond the SM. Neutron EDMs have been an active area of research for a while and many limits have been set through these searches. The most recent study by the Paul Scherrer Institute puts a limit on the neutron EDM at  $|d_n| < 1.8 \times 10^{-26}e.cm$  [13], and helps exclude certain SUSY parameters. Meanwhile, the most recent limit placed on the proton EDM by using  $^{199}\text{Hg}$  stands at  $|d_p| < 7.9 \times 10^{-25}e.cm$  [14].

Equation 1.3 clearly shows that studying the spin of a particle can illuminate aspects on the particle's EDM. EDMs and MDMs are affected by external electromagnetic fields, therefore affecting the spin. The details of the spin dynamics are given later in this thesis. A storage ring can, by definition, store particles for long periods of time allowing the study of spin dynamics. The Cooler Synchrotron is an ideal facility to perform such investigations.

### 1.3 The COoler SYnchrotron (COSY)

The COoler SYnchrotron (COSY) (Fig. 1.2) is a magnetic storage ring in Forschungszentrum Jülich, commissioned in 1993. It consists of the main storage ring, with a circumference of 183.4 m and a beam energy range of 0.3 to 3.7 GeV [15], the sources for the ions, the accelerating cyclotron and the injection

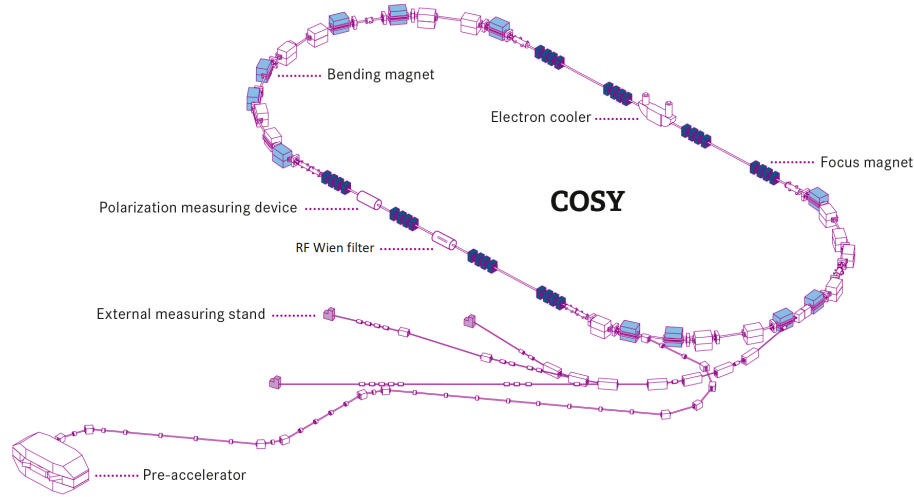


Figure 1.2: Outline of the COSY facility, showing the initial acceleration provided by the cyclotron (labelled in the figure as "pre-accelerator") and the injection beam line leading to the storage ring.

beam line. The details of each component will not be elaborated here since they are beyond the scope of this thesis. A brief overview of the facility is given here.

The beam, of polarized or unpolarized deuterons or protons, is accelerated to specific injection kinetic energies, 45 MeV for  $H^-$  ions and 76 MeV for  $D^-$  ions, using a cyclotron and then injected into the storage ring via the injection beam line. During injection, the ions are stripped of their electrons, therefore, positive ions or particles enter the storage ring. The storage ring is a race-track shape and consists of two straight sections, each of length 40 m, and two curved sections of lengths 52 m each. The synchrotron also accelerates the beam. COSY also has electron and stochastic cooling facilities which are used to bring down the emittance of the beam, and an RF solenoid which is used to manipulate the spins of the particles by subjecting them to an oscillating magnetic field. The beam magnets used to maintain a stable orbit are water-cooled conducting magnets with magnetic fields of up to 1.58T.

The WASA (**W**ide **A**ngle **S**hower **A**pparatus) polarimeter is situated in one of the straight sections. It consists of a fixed carbon target placed along the beam trajectory and four scintillator detector quadrants which are used to measure the polarization of particles. The details of the process will be elaborated in the following chapter. The scattering of a polarized deuteron beam on a neutral target has a cross section which depends on the polarization of particles. Details on the cross section and polarimetry are given in the following chapter.

## 1.4 Outline of the Thesis

The measurement of EDMs depends on having spin polarized particles in storage rings for long periods of time with coherent spin vectors, i.e. maintaining their spatial polarization. A relevant measure in this system is the spin coherence time (SCT), defined as the time taken for the polarization vector to drop to  $e^{-1/2} = 0.606$  of its initial magnitude. Currently, SCTs of the order of  $10^3$  s have been achieved [16]. Another quantity is the spin tune, defined as the ratio between the frequency of spin precession to the frequency of particle revolutions in the ring

$$\nu_s = \frac{f_s}{f_{rev}}. \quad (1.4)$$

In this thesis, data from the May 2019 run, which used a polarized deuteron beam and had cycles of 1000 seconds, is analyzed and the spin tune is measured. Chapter 2 gives the underlying physics of the experiment, the dynamics of the spin and its connection to polarimetry. Chapter 3 describes the methods used to analyze the data as well as provide results of the analysis, while chapter 4 compares the results between different particle bunches in the same cycle.

## Chapter 2

# Spin Dynamics and Polarimetry

### 2.1 Spin and Polarization Formalism

The following is an overview of the formalism used in the case of spin-1/2 particles [17]. A spinor  $\psi$ , with two components, is used to denote a single spin-1/2 particle. The Pauli spin matrices are denoted as a vector  $\boldsymbol{\sigma}$  whose components are the individual matrices

$$\sigma_1 = \begin{pmatrix} 0 & 1 \\ 1 & 0 \end{pmatrix}, \sigma_2 = \begin{pmatrix} 0 & -i \\ i & 0 \end{pmatrix}, \sigma_3 = \begin{pmatrix} 1 & 0 \\ 0 & -1 \end{pmatrix}. \quad (2.1)$$

The spin observable is given by the hermitian operator

$$\hat{\mathbf{S}} = \frac{\hbar}{2} \boldsymbol{\sigma}. \quad (2.2)$$

A density operator is used to define a multi-particle state [18], such as a particle beam

$$\rho = \sum_i f_i |\psi_i\rangle \langle \psi_i|, \quad (2.3)$$

where  $|\psi_i\rangle$  is a finite set of basis vectors and  $f_i$  corresponds to the fraction of particles in a particular state  $i$ . In the particular case of spin-1/2 particles, the density is given by

$$\rho = \frac{1}{2} (1 + \mathbf{P} \cdot \boldsymbol{\sigma}), \quad (2.4)$$

where  $\mathbf{P}$  is the polarization vector, and is defined as

$$\mathbf{P} = \frac{1}{N} \sum_{i=1}^N \mathbf{S}_i, \quad (2.5)$$

summing over the individual particles in the ensemble. In COSY, dipole magnets are used to bend the beam which have vertical magnetic fields and, therefore, the vertical axis becomes the quantization axis for the spins of the particles. In the case of spin-1/2 particles, the vertical polarization is given by

$$P_V = \frac{N^{m=1/2} - N^{m=-1/2}}{N^{m=1/2} + N^{m=-1/2}}, \quad (2.6)$$

where  $N^{m=1/2}$  and  $N^{m=-1/2}$  correspond to the number of particles in each quantization state.

A similar formalism applies to spin-1 particles with some modifications. Spin-1 particles are defined by spinors with three components and have three quantization states:  $m = -1, 0, 1$ . The three spin observables are

$$\hat{S}_1 = \frac{\hbar}{\sqrt{2}} \begin{pmatrix} 0 & 1 & 0 \\ 1 & 0 & 1 \\ 0 & 1 & 0 \end{pmatrix}, \quad \hat{S}_2 = \frac{\hbar}{\sqrt{2}} \begin{pmatrix} 0 & -i & 0 \\ i & 0 & -i \\ 0 & i & 0 \end{pmatrix}, \quad \hat{S}_3 = \frac{\hbar}{\sqrt{2}} \begin{pmatrix} 1 & 0 & 0 \\ 0 & 0 & 0 \\ 0 & 0 & -1 \end{pmatrix}. \quad (2.7)$$

Using these three spin operators, nine independent hermitian matrices are formed which completely describe a spin-1 system. Each matrix can be written as an outer product of the spin operators, and split into a symmetric and an asymmetric part. The set of ten operators is constructed as

$$\hat{S}_{ij} = \frac{3}{2} \left( \hat{S}_i \hat{S}_j + \hat{S}_j \hat{S}_i \right) - 2I \delta_{ij}; \quad i, j \in 1, 2, 3, \quad (2.8)$$

where  $I$  denotes the identity matrix and  $\delta_{ij}$  the Kronecker delta. Nine of the ten operators are independent due to the condition

$$\hat{S}_{11} + \hat{S}_{22} + \hat{S}_{33} = 0. \quad (2.9)$$

If the system is axially symmetric about the quantization axis, as is the case of particles in a storage ring, the density matrix takes the form

$$\rho = \frac{1}{3} \left( I + \frac{3}{2} P_3 \hat{S}_3 + \frac{1}{2} P_{33} \hat{S}_{33} \right), \quad (2.10)$$

where  $P$  is the polarization, and  $P_{ij} = P_{ji}$ . The vector and tensor polarizations are defined as follows, in cartesian coordinates:

$$P_V = \frac{N^{m=1} - N^{m=-1}}{N^{m=1} + N^{m=0} + N^{m=-1}}, \quad (2.11)$$

$$P_T = \frac{N^{m=1} + N^{m=-1} - 2N^{m=0}}{N^{m=1} + N^{m=0} + N^{m=-1}}. \quad (2.12)$$

## 2.2 Spin Dynamics

The spin vector  $\mathbf{S}$  of a particle is affected by external electric and magnetic fields, following a differential equation, in the non-relativistic cases, of the form

$$\frac{d\mathbf{S}}{dt} = \boldsymbol{\Omega} \times \mathbf{S} = \boldsymbol{\mu} \times \mathbf{B} + \mathbf{d} \times \mathbf{E}, \quad (2.13)$$

where  $\boldsymbol{\mu}$  and  $\mathbf{d}$  are the magnetic and electric dipole moments, respectively, defined in eq. 1.3, and  $\mathbf{E}$  and  $\mathbf{B}$  are the electric and magnetic fields in the rest frame of the particle, respectively. The spin precesses with an angular frequency of  $|\boldsymbol{\Omega}|$  [18].

In the case of a an electron, the magnetic moment is given by

$$\boldsymbol{\mu} = g \frac{e}{2m_e} \mathbf{S}, \quad (2.14)$$

the same definition as eq. 1.3. The  $g$ -factor that appears in this definition is a proportionality constant relating the observed magnetic moment of a particle  $\boldsymbol{\mu}$  to its angular momentum quantum number, which appears in  $\mathbf{S}$  as multiple of  $\hbar$ , and a unit of magnetic moment, like the Bohr magneton or nuclear magneton. In the case of protons, nuclei or other baryonic particles, the nuclear magneton  $\mu_N$  is used, therefore using the proton mass instead of the particle mass

$$\boldsymbol{\mu} = g \frac{\mu_N}{\hbar} \mathbf{I} = g \frac{e}{2m_p} \mathbf{I}. \quad (2.15)$$

The anomalous magnetic moment  $G$  arises due to corrections to the magnetic moment by quantum loops. The difference between the magnetic moment calculated using tree level diagrams and the observed magnetic moment is defined as the anomalous magnetic moment

$$G = a = \frac{g - 2}{2}. \quad (2.16)$$

The equation of motion for the spin 2.13 needs to be modified for relativistic cases, as is in a particle accelerator, in the laboratory frame and in curvilinear coordinates. This leads to the Thomas-Bargmann-Michel-Telegdi (Thomas-BMT) equation [19] :

$$\frac{d\mathbf{S}}{dt} = (\boldsymbol{\Omega}_{MDM} + \boldsymbol{\Omega}_{EDM}) \times \mathbf{S}. \quad (2.17)$$

$\boldsymbol{\Omega}_{MDM}$  and  $\boldsymbol{\Omega}_{EDM}$  are the angular frequencies of the magnetic and electric dipole moments, respectively, with the following explicit forms :

$$\boldsymbol{\Omega}_{MDM} = -\frac{q}{m} \left[ \left( G + \frac{1}{\gamma} \right) \mathbf{B} - \frac{G\gamma}{\gamma + 1} (\boldsymbol{\beta} \cdot \mathbf{B}) \boldsymbol{\beta} - \left( G + \frac{1}{1 + \gamma} \right) \boldsymbol{\beta} \times \frac{\mathbf{E}}{c} \right], \quad (2.18)$$

$$\boldsymbol{\Omega}_{EDM} = -\frac{q}{mc} \frac{\eta_{EDM}}{2} \left[ \mathbf{E} - \frac{\gamma}{1 + \gamma} (\boldsymbol{\beta} \cdot \mathbf{B}) \boldsymbol{\beta} + c\boldsymbol{\beta} \times \mathbf{B} \right], \quad (2.19)$$

where  $\gamma$  and  $\boldsymbol{\beta}$  have the usual relativistic definitions, and the electromagnetic fields are defined in the curvilinear laboratory frame.

The Thomas-BMT equation (2.17) describes the precession of the spin about the polarization axis as long as there is a horizontal component of the spin vector, i.e. as long as it is not perfectly aligned with the polarization axis. The spin tune  $\nu_s$  is defined as the number of times the spin precesses about its axis per particle turn in the storage ring, equivalently as the ratio between the spin precession frequency  $f_s$  and the particle revolution frequency  $f_{rev}$  :

$$\nu_s = \frac{f_s}{f_{rev}}. \quad (2.20)$$

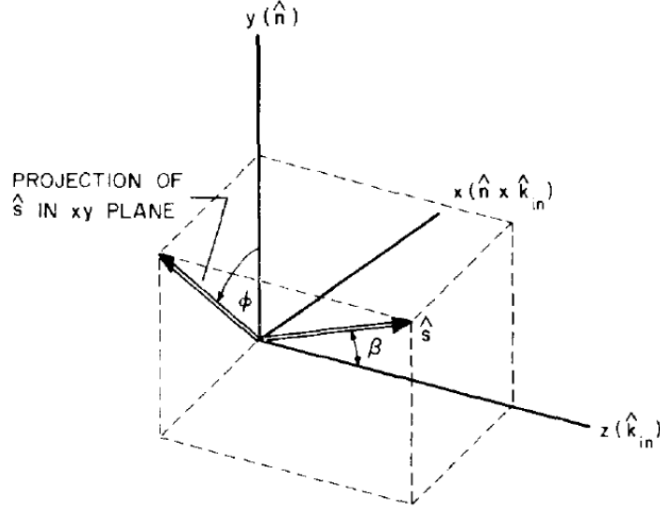


Figure 2.1: The coordinate system used to define the space in which the scattering occurs. Note that the axes have been rotated about the  $y$ -axis compared to the axes in fig. 2.2 in order to clearly show the angles with respect to the positive axes. [20]

### 2.3 Scattering Cross Section and Polarimetry

Figure 2.2 shows a schematic representation of the WASA polarimeter. The coordinate system is defined as follows : the beam travels along the positive  $z$ -axis, the polarization axis is the positive  $y$ -axis, and the right hand rule gives us the positive  $x$ -axis ; the azimuthal angle  $\phi$  is measured from the positive  $y$ -axis to the projection on the  $x - y$  plane and the polar angle  $\theta$  from the positive  $z$ -axis (Fig. 2.1). The detector has 4 quadrants which completely cover the azimuthal angle  $\phi$  around and downstream of the point of scattering, allowing for monitoring the build up of vertical polarization during the experiment. The beam of polarized deuterons is extracted by moving it onto the target, where it scatters elastically. The differential cross section of such an interaction is given by [22]

$$\begin{aligned} \frac{d\sigma}{d\Omega}(\theta, \phi, \beta) = \frac{d\sigma_0}{d\Omega}(\theta) \left[ 1 + 2\frac{\sqrt{3}}{2}P_V \sin \beta \sin \phi iT_{11}(\theta) + \frac{1}{2\sqrt{2}}P_T (3 \cos^2 \beta - 1) T_{20}(\theta) \right. \\ \left. - 2\sqrt{\frac{3}{2}}P_T \sin \beta \cos \beta \cos \phi T_{21}(\theta) \right. \\ \left. + 2\frac{\sqrt{3}}{4}P_T \sin^2 \beta \sin 2\phi iT_{22}(\theta) \right], \end{aligned} \quad (2.21)$$

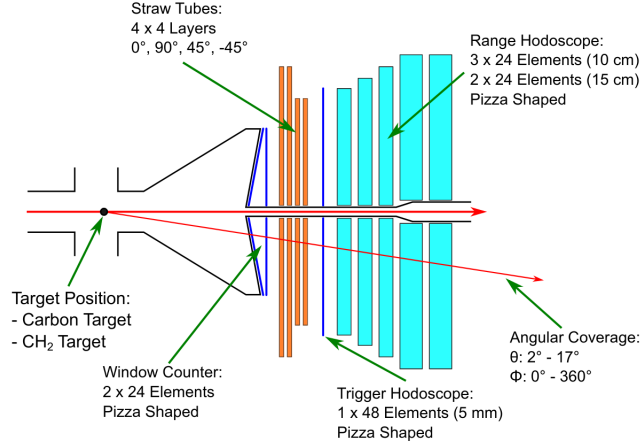


Figure 2.2: WASA polarimeter, showing the four detector quadrants and the target position in the beam pipe. [21]

where  $\beta$  is the polar angle of the detector,  $\sigma_0$  is the unpolarized cross section,  $P_V$  and  $P_T$  are the vector and tensor polarizations, defined in eq. 2.11 and 2.12, and  $iT_{11}$  and  $iT_{2*}$  are the corresponding analyzing powers. For a purely vector polarized beam of intensity  $I$  particles per second scattering off a target of density  $\rho$  and relatively small thickness, the counting rate  $N^{(i)}$  of a detector element  $i$  with solid angle  $\Omega^{(i)}$  is given by

$$\begin{aligned}
 N^{(i)} &= I\rho \int_{\Omega^{(i)}} \frac{d\sigma}{d\Omega}(\theta, \phi, \beta) d\Omega \\
 &= I\rho \int_{\Omega^{(i)}} \frac{d\sigma_0}{d\Omega}(\theta) d\Omega + \sqrt{3}P_V \sin \beta \int_{\Omega^{(i)}} \left[ \frac{d\sigma_0}{d\Omega}(\theta) iT_{11}(\theta) \sin \phi \right] d\Omega \quad (2.22) \\
 &= N_0^{(i)} \left[ 1 + \sqrt{3}P_V \sin \beta A_0^{(i)} \right],
 \end{aligned}$$

where  $N_0^{(i)}$  and  $A_0^{(i)}$  are defined as

$$N_0^{(i)} = I\rho \int_{\Omega^{(i)}} \frac{d\sigma_0}{d\Omega}(\theta) \sin \theta d\theta d\phi, \quad (2.23)$$

$$A_0^{(i)} = \frac{1}{N_0} \int_{\Omega^{(i)}} \left[ \frac{d\sigma_0}{d\Omega}(\theta) iT_{11}(\theta) \sin \phi \right] \sin \theta d\theta d\phi. \quad (2.24)$$

Therefore, for the left and right detectors, i.e at  $\phi = -\frac{\pi}{2}$  and  $\phi = +\frac{\pi}{2}$ , the counting rates are

$$N\left(\phi = -\frac{\pi}{2}\right) = N_0 \left[ 1 - \sqrt{3}P_V \sin \beta A_0 \right], \quad (2.25)$$

$$N\left(\phi = +\frac{\pi}{2}\right) = N_0 \left[ 1 + \sqrt{3}P_V \sin \beta A_0 \right], \quad (2.26)$$

respectively. The relative asymmetry between these two rates,

$$\mathcal{A} = \frac{N\left(\frac{\pi}{2}\right) - N\left(-\frac{\pi}{2}\right)}{N\left(\frac{\pi}{2}\right) + N\left(-\frac{\pi}{2}\right)} = \sqrt{3}P_V A_0 \sin \beta, \quad (2.27)$$

is a measure of vertical polarization  $P_V$  and  $A_0$ , independent of the particle flux. If a detector is shifted by an azimuthal angle  $\phi$  in the laboratory frame and correspondingly  $\Delta\phi$  in the scattering frame, since the two need not be the same,  $\Delta\phi$  is the angle between the plane of the spin vector  $\mathbf{S}$  and the  $y - z$  plane of the laboratory frame. If detectors are then placed at  $+x(\phi = -\frac{\pi}{2})$  and  $-x(\phi = \frac{\pi}{2})$ , the laboratory frame becomes sensitive to the vertical component of the vector polarization  $P_V$  and the associated analyzing power  $\mathcal{A}_{LR}$ , defined as

$$\mathcal{A}_{LR} = \frac{L - R}{L + R} = \sqrt{3}P_V A_0 \sin \beta \cos \Delta\phi = P_V^y A_0. \quad (2.28)$$

$L$  and  $R$  refer to the counting rates in the left and right detectors, respectively (Eq. 2.27). Equivalently, if detectors are kept above and below the beam, at  $\phi = 0$  and  $\phi = \pi$ , the associated analyzing power  $\mathcal{A}_{DU}$  gives a measure of the horizontal component of the vector polarization

$$\mathcal{A}_{DU} = \frac{D - U}{D + U} = P_V A_0 \sin \beta \cos \Delta\phi = P_V^x A_0. \quad (2.29)$$

$U$  and  $D$  are the counting rates of the up and down detectors, respectively. If the particles are injected into the ring with their polarizations all aligned to the vertical axis, then as time progresses and the spin vectors decohere, we will gradually see a build up of the horizontal component of the vertical polarization.

## Chapter 3

# Data Analysis

The data analysed in this thesis was recorded during the April 2019 beam-time in COSY at Forschungszentrum Jülich. The specific run, number 51180, consisted of four cycles, two of which were unpolarized, with a deuteron beam with four bunches. The beam momentum was 0.97 GeV/c. The duration of the cycle was of the order of  $10^3$  seconds and the beam was extracted in ten intervals throughout the cycle (Fig. 3.1). Therefore, only the data during the extraction is analysed and a spin tune behaviour for the entire cycle is extrapolated. This chapter describes the data acquisition process from the polarimeter and the analysis performed on it to extract the spin tune.

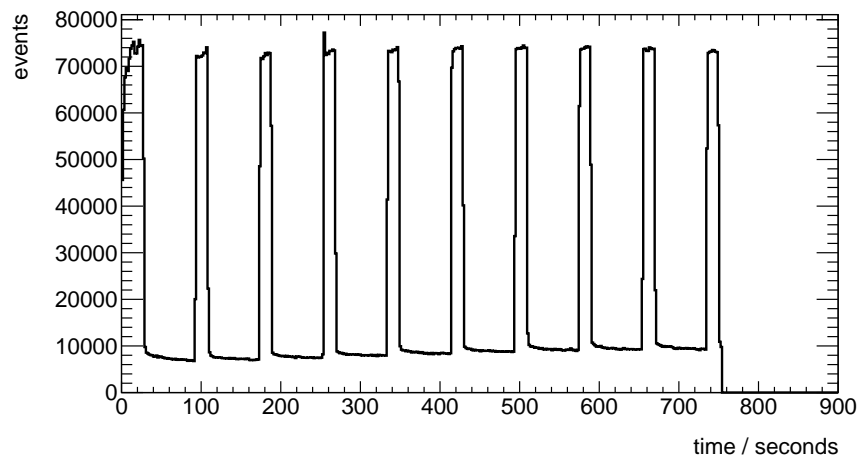


Figure 3.1: Number of events recorded during the cycle being analyzed. The extraction periods, which show a marked increase in the number of events, are considered during the analysis procedure.

### 3.1 Experimental Method and Data Acquisition

The polarized ion source provides hydrogen and deuterium ions of energies 4.5 keV and 7.6 keV, respectively. These ions are then accelerated using the JULIC cyclotron upto their injection energies of 45 MeV for hydrogen and 76 MeV for deuterons respectively (Ref. Chapter 1.3). Before entering the storage ring, the beam is stripped of its charge by a thin carbon foil and enters uncharged. The COSY facility also uses electron cooling to lower the beam emittance. Electron cooling occurs when an electron beam with the same mean longitudinal velocity and smaller transverse velocity momentum spread than the main beam is guided into the trajectory of the main beam and, by Coulomb interaction, the emittance of the ion beam is reduced. The electron beam is then guided out by magnets [23].

The deuteron beam with a momentum of  $p = 970$  MeV/c in COSY, with a circumference of 184 m, corresponds to a frequency of 750.6 kHz and a period of 1.33  $\mu$ s. After each scattering incidence, the scintillators in the polarimeter are hit by light which are detected by the photomultiplier tubes (PMTs). With the addition of these PMT signals and appropriate triggers, this signal is passed from each detector quadrant. All four signals from the quadrants, with respective triggers, are passed to time-to-digital convertors (TDCs) where each trigger signal is recorded as an event. The COSY RF cavity signal, prescaled by a factor of 100, is taken as a reference signal [18]. A detailed explanation of the data acquisition methodology can be found in [24].

The time interval between the initial particle injection and the end of the recording of measurements and a ramp down of the COSY magnets is defined as a cycle, and multiple subsequent cycles with the same beam and accelerator configurations define a run. The run being analyzed in this thesis consisted of 4 cycles, each running for 900 seconds. A brief overview of the experimental procedure is given below, a more detailed treatment is found here [25],

- A vector polarized ion beam is injected into COSY, with initial vertical polarization and three polarization states.
- The beam is accelerated to the momentum of  $p = 970$  MeV/c, after which beam preparation is carried out. Electron cooling reduces the emittances and momentum spread of the beam and a correction of vertical and horizontal orbits is performed.
- After cooling, a vertical orbit bump is applied on the beam to move it to right below the carbon target in WASA.
- The scattering process is initiated. it is guided onto the carbon target and slowly extracted with an efficiency of approximately  $\eta = 10^{-3}$  [26], which translates to one particle out of a thousand being scattered and recorded as an event. The scattering events are recorded continuously for analysis.

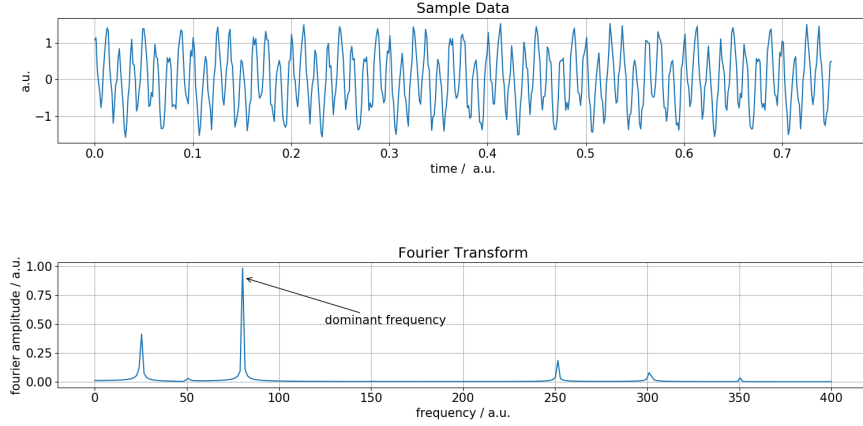


Figure 3.2: Visual representation of the Fourier transform. The sample data shown in the top panel consists of sine waves of different frequencies; the Fourier transform decomposes the signal onto a frequency domain, showing clearly the dominant frequencies with equivalent amplitudes. In a discrete Fourier transform, only discrete samples of the sample data is recorded and used in the transformation procedure, using the formulas discussed in the text.

### 3.1.1 COSY RF-Cavity Signal

The COSY RF-cavity signal is used as a reference signal to determine the horizontal spin precession. The RF-cavity sends a signal to the TDC every one hundred periods. If  $t_{\text{RF},i}$  is the  $i^{\text{th}}$  signal sent by the RF-cavity to the TDC, the period time  $T_{\text{RF},i}$  is determined as

$$T_{\text{RF},i} = \frac{t_{\text{RF},i+1} - t_{\text{RF},i}}{100}. \quad (3.1)$$

The time after the  $j^{\text{th}}$  turn after  $t_{\text{RF},i}$  is given by

$$t_{\text{RF},i,j} = t_{\text{RF},i} + j \cdot T_{\text{RF},i}, \quad j = 0 \dots 99. \quad (3.2)$$

Each event recorded is assigned a turn number  $n \in \mathbb{Z}$ , which is determined by comparing the time of the event  $t_{\text{ev}}$  to  $t_{\text{RF},i}$ . A pre-scale factor is defined as how often the RF-cavity sends a signal to the TDC, therefore,  $n_{\text{ps}} = 100$ . This reduces the fluctuations in the data taking process without compromising on data since it can still account for the observable macroscopic differences in the cavity. The product of the pre-scale factor  $n_{\text{ps}}$  and the number of RF signals  $n_{\text{RF}}$  defines a macroscopic turn interval. The turn number  $n$  is defined as

$$n = n_{\text{ps}} \cdot n_{\text{RF}} + \left\lfloor \frac{t_{\text{ev}} - t_{\text{RF},i}}{T_{\text{RF}}} \right\rfloor. \quad (3.3)$$

$T_{\text{RF}}$  is the period for COSY, which is approximately  $1.336 \mu\text{s}$ . The floor function, shown by the brackets, ensures that the greatest integer value is considered. The

next turn is defined every time the bunch passes through the cavity again. the turn number of the event is independent of  $T_{RF}$  since the reference time  $t_{RF}$  is read out every 100 turns [18]. The main principle of the spin tune analysis is based on assigning each recorded event a turn number, which is guaranteed by the unambiguous determination of particle turn number.

## 3.2 Discrete Turn Fourier Transform

For a function  $f(t)$  in the time domain, the Fourier transform is defined as [27]

$$\tilde{f}(\omega) = \frac{1}{\sqrt{2\pi}} \int_{-\infty}^{\infty} f(t) e^{-i\omega t} dt, \quad (3.4)$$

where  $\tilde{f}(\omega)$  is the transformed function in the (angular) frequency domain. If the motion of the particle spin is described by a simple periodic function  $f(t) = A \cos(\omega_s t + \phi_s)$ , where  $\omega_s$  denotes the angular frequency of the spin and  $\phi_s$  the phase,  $\tilde{f}(\omega)$  is the transformed function in the frequency domain with a peak at the spin tune frequency [18].

In the case of the experiment conducted at COSY, the function  $f(t)$  is discrete since each event is assigned a turn number  $n \in \mathbb{N}$ . Therefore, a discrete Fourier transform is performed on the data which is dependent on the turn number. The function  $f(t)$  is multiplied with a delta comb, formed by summing Dirac delta functions.

$$\tilde{f}(\omega) = \int_{-\infty}^{\infty} \sum_{n=0}^{\infty} f(t) \delta\left(t - \frac{n}{f_{RF}}\right) e^{-it\omega} dt. \quad (3.5)$$

$f_{RF}$  is the RF frequency of the cavity with the relation  $\omega_{RF} = 2\pi f_{RF}$ . Performing the integration over the delta function leads to a discrete function dependent on the turn number,  $f[n]$ , which is summed over for different values of the turn number [18].

$$\begin{aligned} \tilde{f}(\omega) &= \sum_{n=0}^{\infty} f[n] e^{-\frac{in\omega}{f_{RF}}} \\ &= \sum_{n=0}^{\infty} f[n] \left[ \cos\left(\frac{n\omega}{f_{RF}}\right) - i \sin\left(\frac{n\omega}{f_{RF}}\right) \right]. \end{aligned} \quad (3.6)$$

Using the relations  $f_{RF} = \frac{\omega_{RF}}{2\pi}$  and  $\nu = \frac{\omega}{\omega_{RF}}$ , we get

$$\tilde{f}(\nu) = \sum_{n=0}^{\infty} f[n] [\cos(2\pi n\nu) - i \sin(2\pi n\nu)], \quad (3.7)$$

where  $f[n] = A \cos(2\pi\nu_s n + \phi_s)$ . The data, collected in a finite time interval, is described using a rectangular window function  $w[n]$ . If  $N$  is the last turn

number in the measurement interval,  $w[n]$  is defined as

$$w[n] = \begin{cases} 0 & n < 0 \\ 1 & 0 \leq n < N \\ 0 & n \geq N \end{cases} . \quad (3.8)$$

Multiplication in the turn number domain  $g[n] = f[n] \cdot w[n]$  corresponds to convolution in the spin tune domain  $\tilde{g}(\nu) = \tilde{f}(\nu) * \tilde{w}(\nu)$ . This leads to

$$\begin{aligned} \tilde{g}(\nu) &= \tilde{f}(\nu) * \tilde{w}(\nu) \\ &= \int_{-\infty}^{\infty} \tilde{f}(\nu - \lambda) \tilde{w}(\lambda) d\lambda \\ &= \sum_{n=0}^{\infty} f[n] w[n] e^{-i2\pi n\nu} \\ &= \sum_{n=0}^{N-1} g[n] e^{-i2\pi n\nu} . \end{aligned} \quad (3.9)$$

The discrete Fourier transforms of the functions  $f[n]$  and  $w[n]$  are as follows

$$\tilde{f}(\nu) = \frac{A}{2} (\delta(\nu - \nu_s) + \delta(\nu + \nu_s)) , \quad (3.10)$$

$$\tilde{w}(\nu) = \sum_{n=0}^{N-1} e^{-i2\pi n\nu} = \frac{1 - e^{-i2\pi N\nu}}{1 - e^{-i2\pi\nu}} . \quad (3.11)$$

Therefore, substituting in eq. 3.9,

$$\tilde{g}(\nu) = \frac{A}{2} \int_{-\infty}^{\infty} (\delta(\lambda - \nu + \nu_s) + \delta(-\lambda + \nu + \nu_s)) \frac{1 - e^{-i2\pi\lambda N}}{1 - e^{-i2\pi\lambda\nu}} d\lambda . \quad (3.12)$$

However, it is not possible to have a perfectly continuous distribution in the spin tune domain since the consecutive values of  $\nu$  cannot be infinitesimally close to each other. Consequently, the spin tune domain becomes discrete with a sampling interval is given by  $\Delta\nu_k = \frac{1}{N}$ , with  $\nu_k = \frac{k}{N}$  where  $k \in \mathbb{Z}$ . As a result, the discrete turn number signal is discretely transformed into the spin tune domain as

$$\begin{aligned} g_{\nu_k} &= \sum_{n=0}^{N-1} g[n] e^{-i2\pi n\nu_k} \\ &= \sum_{n=0}^{N-1} g[n] (\cos(2\pi n\nu_k) - i \sin(2\pi n\nu_k)) . \end{aligned} \quad (3.13)$$

The turn number signal  $g[n]$  is based on random processes, and the probability of detecting an event per turn is small, therefore,  $g[n]$  is defined as

$$g[n] = \begin{cases} 1 & n = n(n_{ev}) \\ 0 & \text{else} \end{cases} . \quad (3.14)$$

Therefore, the summation over turn number is converted into one over the number of events  $n_{ev} \in [1, N_{ev}]$ . The discrete Fourier coefficients are given by the real and imaginary parts of  $g_{\nu_k}$  :

$$\begin{aligned} a_{\nu_k} &= \mathbb{R}(g_{\nu_k}) = \frac{2}{N_{ev}} \sum_{n_{ev}=1}^{N_{ev}} \cos(2\pi\nu_k n(n_{ev})), \\ b_{\nu_k} &= \mathbb{I}(g_{\nu_k}) = \frac{2}{N_{ev}} \sum_{n_{ev}=1}^{N_{ev}} -\sin(2\pi\nu_k n(n_{ev})), \end{aligned} \quad (3.15)$$

where  $\frac{2}{N_{ev}}$  is a normalization factor. The uncertainty in the Fourier parameters is given by

$$\begin{aligned} \sigma_{a_{\nu_k}} &= \frac{2}{N_{ev}} \sqrt{\sum_{n_{ev}=1}^{N_{ev}} \cos^2(2\pi\nu_k n(n_{ev}))}, \\ \sigma_{b_{\nu_k}} &= \frac{2}{N_{ev}} \sqrt{\sum_{n_{ev}=1}^{N_{ev}} \sin^2(2\pi\nu_k n(n_{ev}))}. \end{aligned} \quad (3.16)$$

The amplitude and phase of the Fourier spectrum is defined as

$$\epsilon_{\nu_k} = |g_{\nu_k}| = \sqrt{\mathbb{R}(g_{\nu_k})^2 + \mathbb{I}(g_{\nu_k})^2} = \sqrt{a_{\nu_k}^2 + b_{\nu_k}^2}, \quad (3.17)$$

$$\phi_{\nu_k} = \arg(g_{\nu_k}) = \text{atan2}(\mathbb{I}(g_{\nu_k}), \mathbb{R}(g_{\nu_k})) = \text{atan2}(b_{\nu_k}, a_{\nu_k}), \quad (3.18)$$

respectively, with the following statistical errors

$$\begin{aligned} \sigma_{\epsilon_{\nu_k}} &= \sqrt{\frac{a_{\nu_k}^2 \sigma_{a_{\nu_k}}^2 + b_{\nu_k}^2 \sigma_{b_{\nu_k}}^2}{a_{\nu_k}^2 + b_{\nu_k}^2}}, \\ \sigma_{\phi_{\nu_k}} &= \sqrt{\frac{a_{\nu_k}^2 \sigma_{b_{\nu_k}}^2 + b_{\nu_k}^2 \sigma_{a_{\nu_k}}^2}{(a_{\nu_k}^2 + b_{\nu_k}^2)^2}}. \end{aligned} \quad (3.19)$$

The cycle, consisting of  $\sim 600 \cdot 10^6$  turns, is divided into segments. Using a selected frequency range, each event with a specific turn number  $n$  is used to calculate the Fourier coefficients according to equation 3.15, the corresponding coefficients are filled into a histogram. A reference is used, in this case the number of events in the up detector, in order to analyze events only during the extraction periods. The number of events in the four detector quadrants show clearly the extraction periods with an increase in the number of events (Fig. 3.3). In order to calculate the amplitude, for each macroscopic interval in time (turn number), a frequency range is scanned and for each frequency the Fourier coefficients from each spectrum plot is used. In fig. 3.5, the amplitudes in different frequency ranges are shown. The details about the phase plots are explained in the next section.

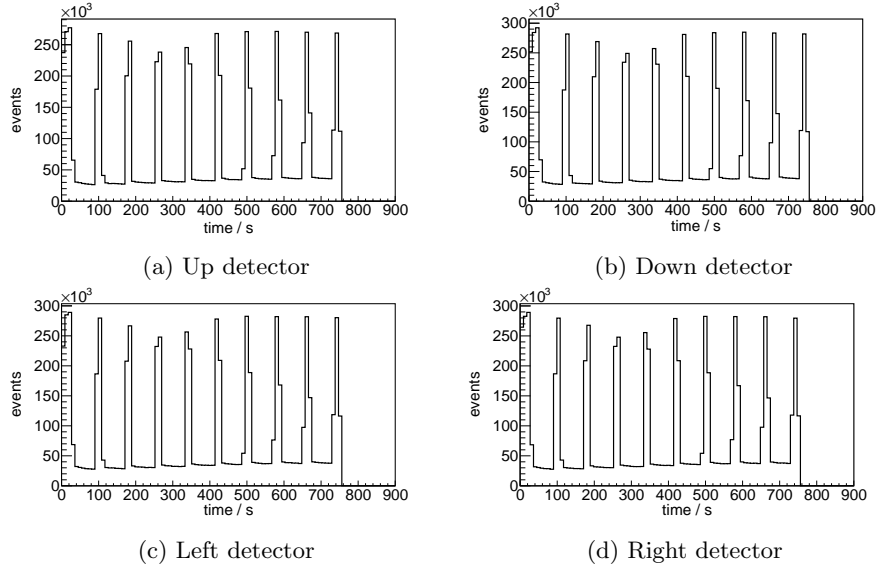


Figure 3.3: The number of events recorded in the four detector quadrants, used as a reference for the analysis with appropriate thresholds.

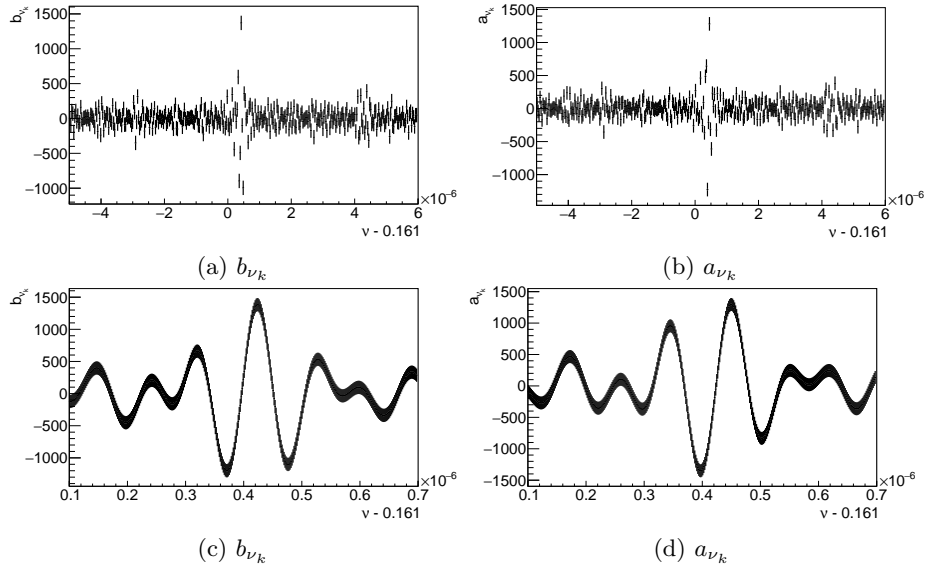


Figure 3.4: Fourier spectrum in the first macroscopic turn bin seen in two frequency ranges of different orders. The top row shows a frequency range of  $10^{-5}$  and the lower row a range of  $10^{-8}$ . Note that the  $x$ -axes have been offset by a frequency value of 0.161 to make them easier to read.

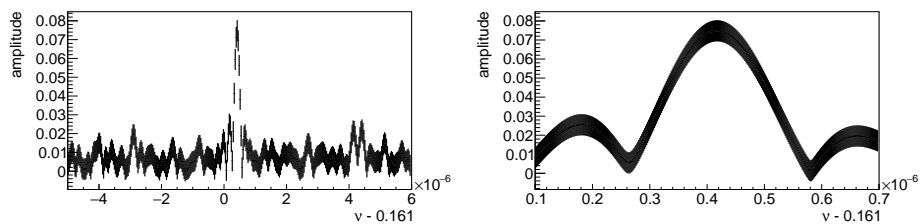


Figure 3.5: Amplitude of the Fourier transform in the 2nd turn bin in different frequency ranges. Note that both  $x$ -axes are offset by 0.161.

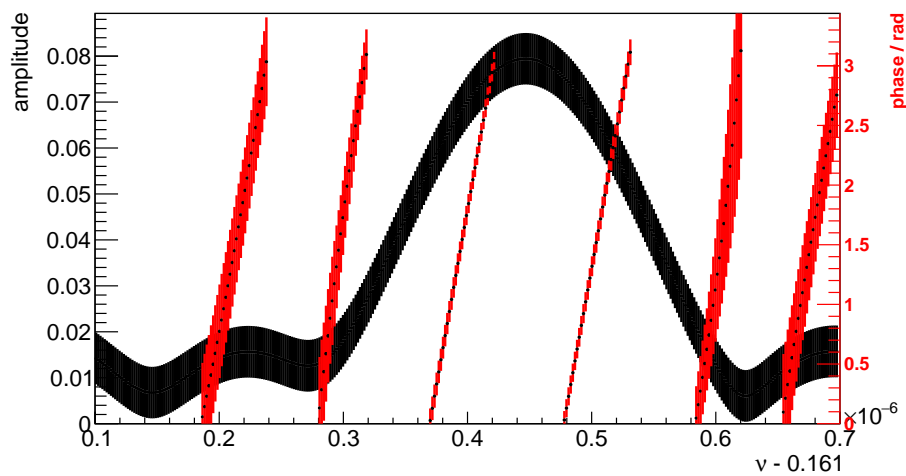


Figure 3.6: Amplitude and phase of the Fourier spectrum. The  $y$ -axis on the left, in black, shows amplitude, and the one on the right, in red, shows phase. Note the  $x$ -axis offset.

### 3.3 Spin Tune Measurement

The probability distribution function describing the incidence of recording particles in the up or down detectors is given by  $p_n(n)$  :

$$p_n(n; \epsilon, \nu_s, \phi_{\nu_s}) = \frac{1}{\Delta n} [1 \pm \epsilon \sin(2\pi\nu_s n + \phi_{\nu_s})], n \in (0, \Delta n), \Delta n \in \mathbb{Z}, \quad (3.20)$$

where  $\phi_{\nu_s}$  is the phase of the spin tune and  $\epsilon = |A_y|P_V$  is the analyzing power times the fraction of vector polarized particles in the ensemble, which depends on the atomic source [18]. The spin tune  $\nu_s$  is assumed to be known and is the same for all particles in the ensemble, the up and down detectors are considered by the plus and minus signs, respectively, and they are assumed to be out of phase by  $\pi$  radians.

The turn depending spin tune  $\nu_s(n)$  is needed to describe the behaviour of the spin tune throughout the cycle. It can be derived from the angular frequency, which is related to the spin tune by a factor of  $2\pi$  and can be extracted from the phase of the Fourier spectrum. The variation in the spin tune is thus

$$\delta\nu_s(n) = \frac{1}{2\pi} \delta\omega_{\nu_s}(n) = \frac{1}{2\pi} \frac{d\delta\phi_{\nu_s}(n)}{dn}. \quad (3.21)$$

The turn dependent spin tune is defined as

$$\nu_s(n) = \nu_s^0 + \delta\nu_s(n) = \nu_s^0 + \frac{1}{2\pi} \frac{d\delta\phi_{\nu_s}(n)}{dn}, \quad (3.22)$$

where  $\nu_s^0$  is the assumed spin tune that remains constant throughout the cycle. The spin tune  $\nu_s$  is equivalently defined as the ratio between the spin precession frequency and the RF frequency

$$\begin{aligned} \nu_s = \frac{f_s}{f_{RF}} &\Rightarrow \frac{\Delta\nu_s}{\nu_s} = \frac{\Delta f_s}{f_s} - \frac{\Delta f_{RF}}{f_{RF}} \\ &= \frac{\frac{\partial\phi_s}{\partial t}}{2\pi f_s} - \frac{\frac{\partial\phi_{RF}}{\partial t}}{2\pi f_{RF}} \\ &= \frac{1}{2\pi\nu_s} \frac{\partial\phi_s}{\partial n}. \end{aligned} \quad (3.23)$$

Therefore, using equations 3.29 and 3.23, we arrive at

$$\begin{aligned} \frac{\nu_s(n)}{\nu_s^0} &= 1 + \frac{\delta\nu_s(n)}{\nu_s^0} \\ &= 1 + \frac{\delta f_s(n)}{f_s} - \frac{\delta f_{RF}(n)}{f_{RF}} \\ &= 1 + \frac{1}{2\pi\nu_s^0} \frac{\partial\phi_s}{\partial n} \end{aligned} \quad (3.24)$$

$$\Rightarrow \nu_s(n) = \nu_s^0 + \frac{1}{2\pi} \frac{\partial\phi_s}{\partial n}. \quad (3.25)$$

Using the phase, the spin tune behaviour for the entire cycle can be interpolated. The phase of the Fourier spectrum is plotted by scanning a frequency range, and for each frequency, the corresponding Fourier coefficients from the spectrum are used. Therefore, each phase plot has a scanning frequency which remains constant throughout the cycle  $\nu_s^0$ . The frequency range is determined by taking the frequency at which the Fourier amplitude reaches its maximum and forming an equal interval before and after that frequency. To smoothen out the phase plots, the difference between two consecutive phase measurements  $\Delta\phi = \phi(n) - \phi(n-1)$  is used to unwrap the phase using the following criteria:

$$\begin{aligned}\phi(n) &= \phi(n) - 2\pi \text{ if } \Delta\phi > \pi, \\ \phi(n) &= \phi(n) + 2\pi \text{ if } \Delta\phi < -\pi.\end{aligned}\tag{3.26}$$

If the scanning frequency for the phase is higher than the true spin tune frequency, the phase difference between the two increases with time, and vice versa in the case of a scanning frequency which is lower than the true spin tune frequency. This also resets when the phase difference is a multiple of  $\pi$ . Therefore, when the scanning frequency matches the spin tune frequency, the phase difference remains constant, i.e.  $\frac{\partial\phi}{\partial n}$  remains constant, and a constant phase can be observed. This can be seen in Fig. 3.7. A better fit can be performed when the spin tune does not remain stable for the entire cycle, since the slope would have to be zero. An appropriate phase plot is selected and fitted with a polynomial, here of order two, in order to extract the turn dependent slope  $\frac{\partial\phi_s}{\partial n}$ . Therefore, if a polynomial

$$\phi_s(n) = an^2 + bn + c\tag{3.27}$$

is fitted (refer fig. 3.8), where  $a$ ,  $b$  and  $c$  are the fit parameters, the slope is given by

$$\frac{\partial\phi_s(n)}{\partial n} = 2an + b.\tag{3.28}$$

Therefore, the turn dependent spin tune has the form

$$\nu_s(n) = \nu_s^0 + \frac{1}{2\pi} (2an + b),\tag{3.29}$$

which has a linear dependence on the turn number.

### 3.4 Uncertainty in the Spin Tune

The uncertainty in the spin tune  $\sigma_{\nu_s}$  can be calculated using standard error propagation, using the errors of the fit parameters,  $\sigma_a$  and  $\sigma_b$ , and the covariance  $\text{cov}(a, b)$  between the fit parameters:

$$\sigma_{\nu_s}^2 = \left( \frac{1}{2\pi} \sigma_{\frac{\partial\phi_s}{\partial n}} \right)^2 = \frac{1}{4\pi^2} (2\sigma_a^2 n + \sigma_b^2 + 4\text{cov}(a, b))\tag{3.30}$$

$$\Rightarrow \sigma_{\nu_s} = \frac{1}{2\pi} \sqrt{2\sigma_a^2 n + \sigma_b^2 + 4\text{cov}(a, b)}.\tag{3.31}$$

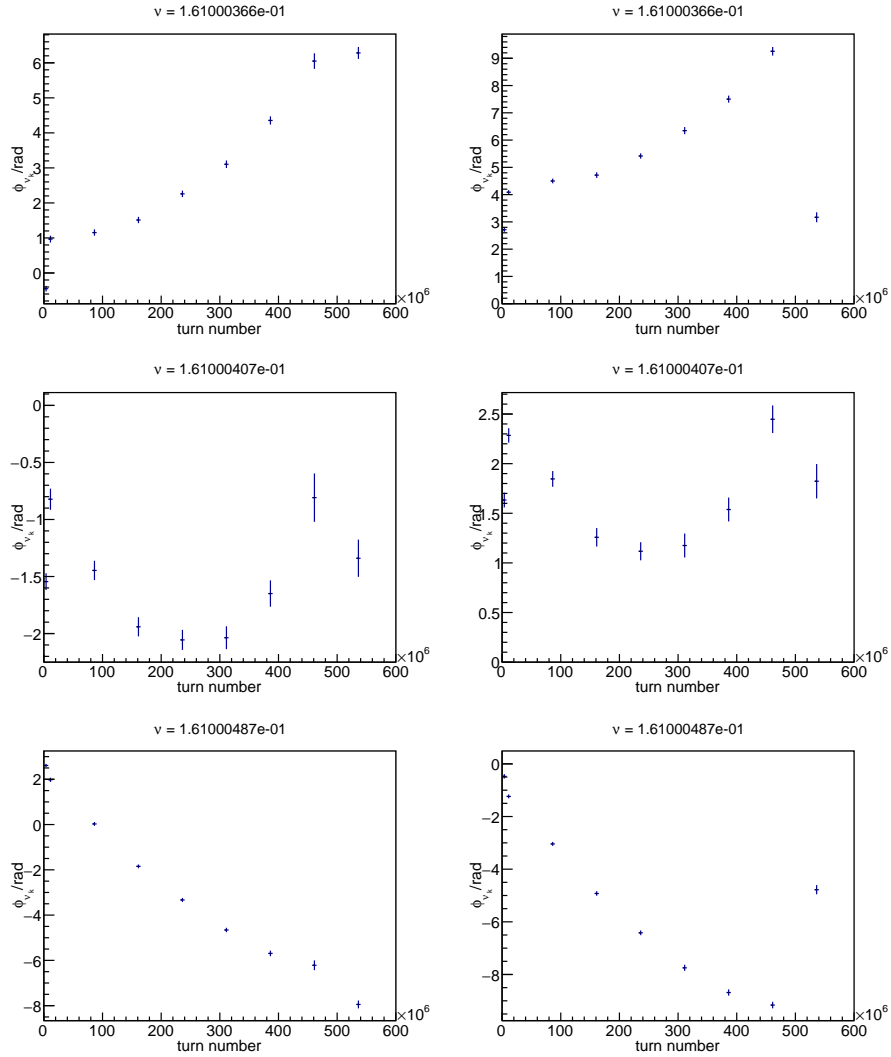


Figure 3.7: The phase of the Fourier transform at different frequencies, shown as the title of the plots. The left hand column is from the up detector and the right hand one from the down detector. When the scanning frequency is different from the spin tune frequency, the phase difference continues to change throughout the cycle, as seen in the top and bottom rows. In the row in the middle, the scanning frequency is close to the true spin tune frequency, therefore the phase is more stable. Note the different  $y$ -axes in the plots.

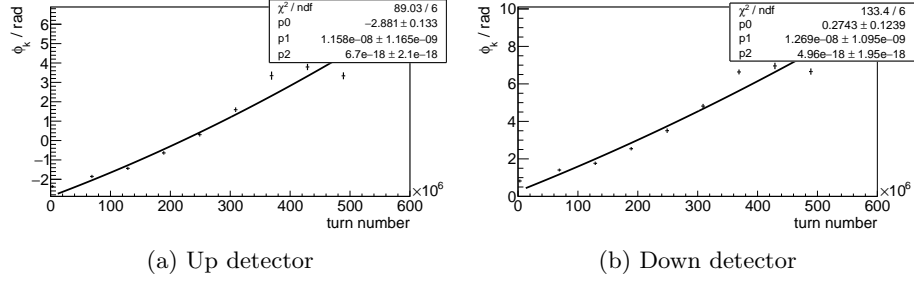


Figure 3.8: The phase of the Fourier spectrum at a fixed spintune value of  $\nu_s^0 = 0.161\,000\,425$  and fitted with a second order polynomial. The fit parameters  $p^X$  correspond to the coefficients of  $n^X$  in the second order polynomial.

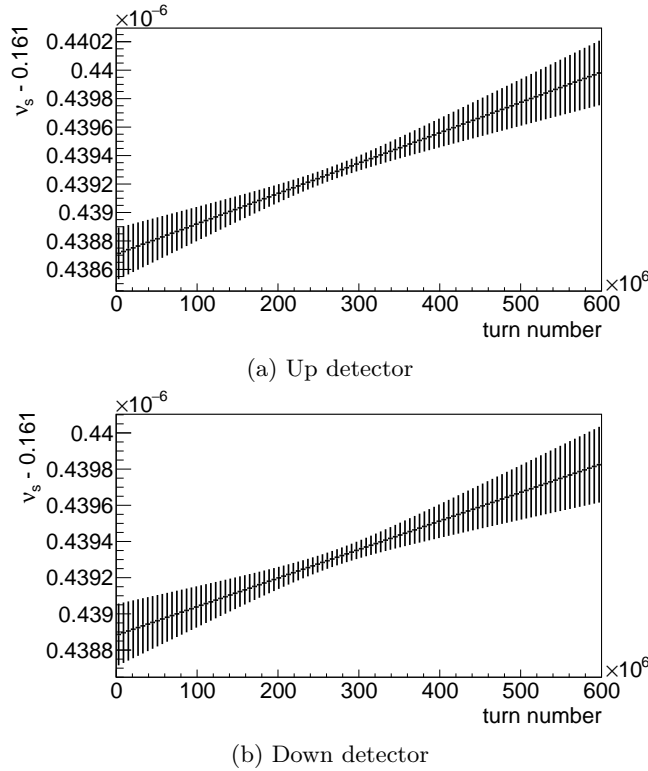


Figure 3.9: The spin tune determined from the phase plots in fig. 3.8 in the up and down detectors. Note the offset in the frequencies in the  $y$ -axes.

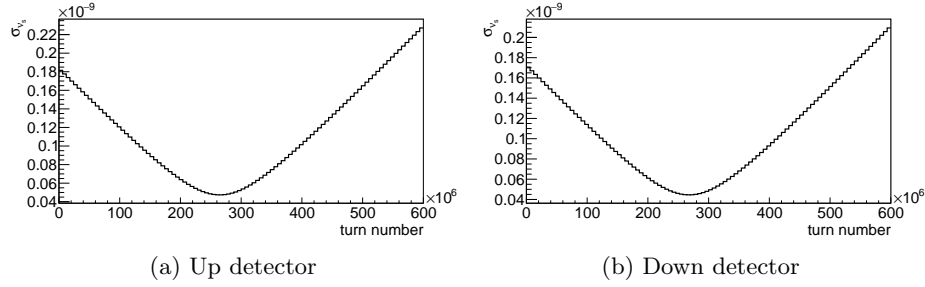


Figure 3.10: The uncertainty in the spin tune in the two detectors

Therefore, we see that the uncertainty in the spin tune  $\sigma_{\nu_s} \propto n^{\frac{1}{2}}$ . The theoretical uncertainty in the spin tune can be calculated by using the method of maximum likelihood [28]. The count rates in the up and down detectors is given by

$$N_{\uparrow,\downarrow}(t) = N_0 (1 \pm P \sin(\omega t + \phi)), \quad (3.32)$$

where  $N_0$  denotes the unpolarized cross section, the up and down detectors are described by the top and bottom signs respectively, the spin precession frequency  $\omega = 2\pi\nu f_{rev}$  where  $f_{rev}$  is the frequency of revolution, and  $P$  denotes the product of the analyzing power and polarization. In order to determine the frequency, polarization and phase from the count rate, an asymmetry of the form

$$A(t) = \frac{N_{\uparrow} - N_{\downarrow}}{N_{\uparrow} + N_{\downarrow}} = P \sin(\omega t + \phi) \quad (3.33)$$

can be formed and fitted with a function  $f(t)$ . However, that is not possible due to the low number of events recorded per second which would provide the statistics to perform such a fit. For deuterons of momentum  $p = 970$  MeV, the Lorentz factor  $\gamma = 1.12$ , spin tune  $\nu = 0.16$  and a revolution frequency of  $f_{rev} = 748$  kHz, therefore a frequency of  $\omega = 752.4$  kHz is obtained. If COSY records one event per millisecond, it will record less than one hundredth of a period. Therefore, the likelihood method is used. The log-likelihood function reads as

$$\begin{aligned} \ell = \log \mathcal{L} = & \sum_{\uparrow} \log [N_0 (1 + P \sin(\omega t_i + \phi))] \\ & + \sum_{\downarrow} \log [N_0 (1 - P \sin(\omega t_i + \phi))] \\ & - [N_{\uparrow}(\omega, \phi, P) + N_{\downarrow}(\omega, \phi, P)] \end{aligned} \quad (3.34)$$

Since the number of events in the detectors is not fixed, the extended maximum likelihood method is used [29], from which the last two terms in eq. 3.34 appear.

The number of events in the up and down detectors is given by

$$\begin{aligned}
 N_{\uparrow,\downarrow}(\omega, \phi, P) &= \int_{t_i}^{t_f} N_{\uparrow,\downarrow}(t) dt \\
 &= N_0 \left[ (t_f - t_i) \pm \frac{P}{\omega} (\cos(\omega t_i + \phi) - \cos(\omega t_f + \phi)) \right] \\
 &= N_0 \left[ (t_f - t_i) \pm \frac{2P}{\omega} \sin\left(\frac{\omega(t_i - t_f)}{2}\right) \sin\left(\frac{\omega(t_i + t_f)}{2} + \phi\right) \right] \\
 &\approx N_0(t_f - t_i),
 \end{aligned} \tag{3.35}$$

where the approximation in the last step holds when  $(t_f - t_i) \gg \frac{1}{\omega}$ . This clearly holds since  $\omega = 752.4 \text{ kHz} \Rightarrow \omega^{-1} = 1.329 \mu\text{s}$ . Therefore,  $N_{\uparrow,\downarrow}(\omega, \phi, P)$  is independent of  $\omega$ ,  $\phi$  and  $P$ , and can be ignored. To find the maximum likelihood estimators we need the first derivatives of the likelihood function with respect to the three independent variables, and the second derivatives for their respective uncertainties. The first derivatives are as follows, each set to zero to find the maxima :

$$\frac{\partial \ell}{\partial \omega} = \sum_i \frac{\pm P t_i \cos(\omega t_i + \phi)}{1 \pm P \sin(\omega t_i + \phi)} \stackrel{!}{=} 0, \tag{3.36}$$

$$\frac{\partial \ell}{\partial \phi} = \sum_i \frac{\pm P \cos(\omega t_i + \phi)}{1 \pm P \sin(\omega t_i + \phi)} \stackrel{!}{=} 0, \tag{3.37}$$

$$\frac{\partial \ell}{\partial P} = \sum_i \frac{\pm \sin(\omega t_i + \phi)}{1 \pm P \sin(\omega t_i + \phi)} \stackrel{!}{=} 0. \tag{3.38}$$

The second derivatives are:

$$\frac{\partial^2 \ell}{\partial \omega^2} = - \sum_i \frac{P t_i^2 (P \pm \sin(\omega t_i + \phi))}{[1 \pm P \sin(\omega t_i + \phi)]^2}, \tag{3.39}$$

$$\frac{\partial^2 \ell}{\partial \phi^2} = - \sum_i \frac{P (P \pm \sin(\omega t_i + \phi))}{[1 \pm P \sin(\omega t_i + \phi)]^2}, \tag{3.40}$$

$$\frac{\partial^2 \ell}{\partial P^2} = - \sum_i \frac{\sin^2(\omega t_i + \phi)}{[1 \pm P \sin(\omega t_i + \phi)]^2}, \tag{3.41}$$

$$\frac{\partial^2 \ell}{\partial \omega \partial \phi} = - \sum_i \frac{P t_i [P \pm \sin(\omega t_i + \phi)]}{[1 \pm P \sin(\omega t_i + \phi)]^2}, \tag{3.42}$$

$$\frac{\partial^2 \ell}{\partial \omega \partial P} = \sum_i \frac{\pm t_i \cos(\omega t_i + \phi)}{[1 \pm P \sin(\omega t_i + \phi)]^2}, \tag{3.43}$$

$$\frac{\partial^2 \ell}{\partial \phi \partial P} = \sum_i \frac{\pm \cos(\omega t_i + \phi)}{[1 \pm P \sin(\omega t_i + \phi)]^2}. \tag{3.44}$$

Using the expectation values of these second derivatives, we can calculate the covariance matrix elements between the three variables

$$(\text{cov}^{-1})_{ij} = -\left\langle \frac{\partial^2 \ell}{\partial a_i \partial a_j} \right\rangle = -\int_0^T N(t) \cdot \frac{\partial^2 \ell}{\partial a_i \partial a_j} \cdot dt, \quad (3.45)$$

where the integration runs over the entire time interval of the measurement cycle, and  $(a_1, a_2, a_3) = (\omega, \phi, P)$ .

$$\left\langle \frac{\partial^2 \ell}{\partial \omega^2} \right\rangle = -\int_0^T N_0(1 \pm P \sin(\omega t + \phi)) \left( \frac{Pt^2(P \pm \sin(\omega t + \phi))}{[1 \pm P \sin(\omega t + \phi)]^2} \right) \cdot dt. \quad (3.46)$$

Making a few approximations, this integral can be solved quite easily. For simplicity, we will consider only the up detector in the following discussion, to make the signs easier to handle. For the down detector, all the following results will hold by replacing  $P$  with  $-P$ . The polarization  $P \ll 1$ , and as mentioned earlier  $\omega T \gg 1$ . The sine and cosine terms average zero over one period and the square terms contribute a factor of one half, therefore,

$$\begin{aligned} \left\langle \frac{\partial^2 \ell}{\partial \omega^2} \right\rangle &= -\int_0^T N_0(1 + P \sin(\omega t + \phi)) \left( \frac{Pt^2(P + \sin(\omega t + \phi))}{[1 + P \sin(\omega t + \phi)]^2} \right) \cdot dt \\ &\approx -N_0 P \int_0^T t^2 (P + \sin(\omega t + \phi))(1 - P \sin(\omega t + \phi)) \cdot dt \\ &= -\frac{N_0 P^2}{2} \int_0^T t^2 \cdot dt \\ &= -\frac{N_0 P^2 T^3}{6} = -\frac{N(PT)^2}{6}, \end{aligned} \quad (3.47)$$

where  $N = N_0 T$ . Similarly for the rest of the expectation values:

$$\left\langle \frac{\partial^2 \ell}{\partial \phi^2} \right\rangle = \frac{NP^2}{2}, \quad (3.48)$$

$$\left\langle \frac{\partial^2 \ell}{\partial P^2} \right\rangle = -\frac{N}{2}, \quad (3.49)$$

$$\left\langle \frac{\partial^2 \ell}{\partial \omega \partial \phi} \right\rangle = -\frac{NP^2 T}{4}, \quad (3.50)$$

$$\left\langle \frac{\partial^2 \ell}{\partial \omega \partial P} \right\rangle = 0, \quad (3.51)$$

$$\left\langle \frac{\partial^2 \ell}{\partial \phi \partial P} \right\rangle = 0. \quad (3.52)$$

Therefore, the covariance matrix has the following form

$$\text{cov}^{-1} = \begin{pmatrix} \frac{N(PT)^2}{6} & \frac{NP^2 T}{4} & 0 \\ \frac{NP^2 T}{4} & \frac{NP^2}{2} & 0 \\ 0 & 0 & \frac{N}{2} \end{pmatrix} \quad (3.53)$$

$$\Rightarrow \text{cov} = \begin{pmatrix} \frac{24}{N((PT)^2)} & \frac{12}{NP^2T} & 0 \\ \frac{12}{NP^2T} & \frac{8}{NP^2} & 0 \\ 0 & 0 & \frac{2}{N} \end{pmatrix} \quad (3.54)$$

The statistical errors on the three parameters correspond to the diagonal elements of the covariance matrix, therefore,

$$\sigma_\omega^2 = \frac{24}{N(PT^2)}, \quad (3.55)$$

$$\sigma_\phi^2 = \frac{8}{NP^2}, \quad (3.56)$$

$$\sigma_P^2 = \frac{2}{N}. \quad (3.57)$$

Therefore, according to eq. 3.55,  $\sigma_\omega \propto T^{-1} \Rightarrow \sigma_\nu \propto T^{-1}$ . Note here that  $T$  is the length of the time for the entire cycle. In [30], it was seen that a 100 s cycle could measure the spin tune to a precision of  $10^{-10}$ . In the cycle analyzed in this thesis of 1000 s, from fig. 3.10 it can be seen that the uncertainty in the spin tune is of the order of  $10^{-11}$ , which agrees with what is expected from eq. 3.55.

## Chapter 4

# Comparison Between Bunches

The run from April 2019, that has been analyzed in this thesis, utilized a deuteron beam which contained four particle bunches. In this chapter, the results presented show the bunch wise comparison of the results obtained. Ion sources often produce particles in a continuous stream, all of which are not accelerated due to the alternating nature of accelerating field. Therefore, particles are bunched in groups. This helps to increase the intensity of particles in the bunch and efficiently accelerate enough particles to undertake the experiment. The particle beam is bunched by passing it through an RF-cavity before it is accelerated to relativistic velocities. In Fig. 4.1 (b), we can see that particles right before the origin, at  $\varphi = 0$  and  $\Delta E_{\text{kin}} = 0$ , have been accelerated by a certain amount, however, the particles right after the origin have been accelerated less. This causes the particles to bunch around that phase. The phase of the RF-cavity determines the characteristics of the bunches. A detailed discussion on particle bunching can be found in [31].

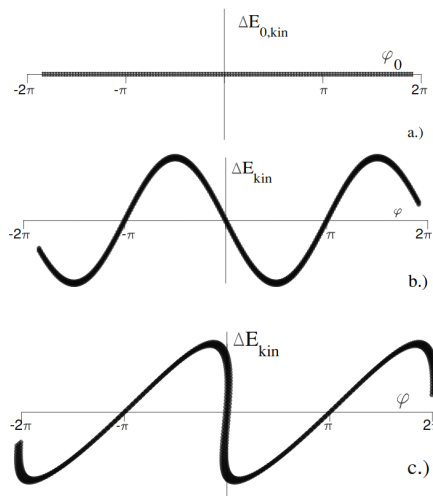


Figure 4.1: The three figures show a particle beam (a) before bunching, having a continuous distribution in phase and energy (a), (b) after bunching, showing sinusoidal energy variation, and (c) strong bunching after the cavity [31]

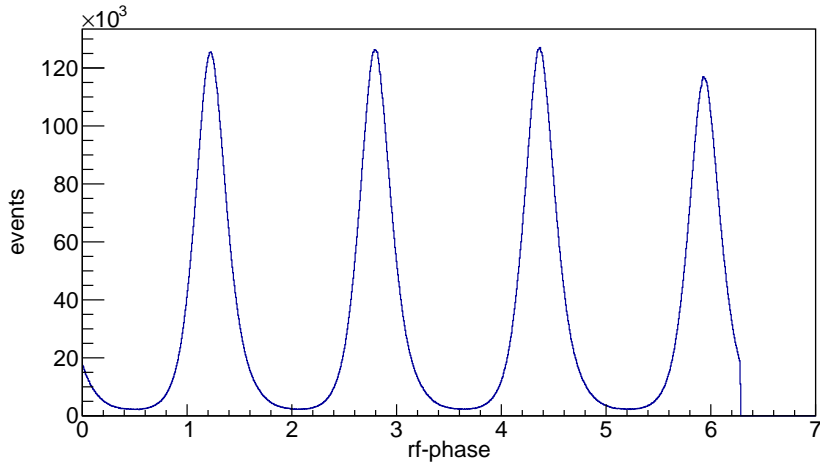
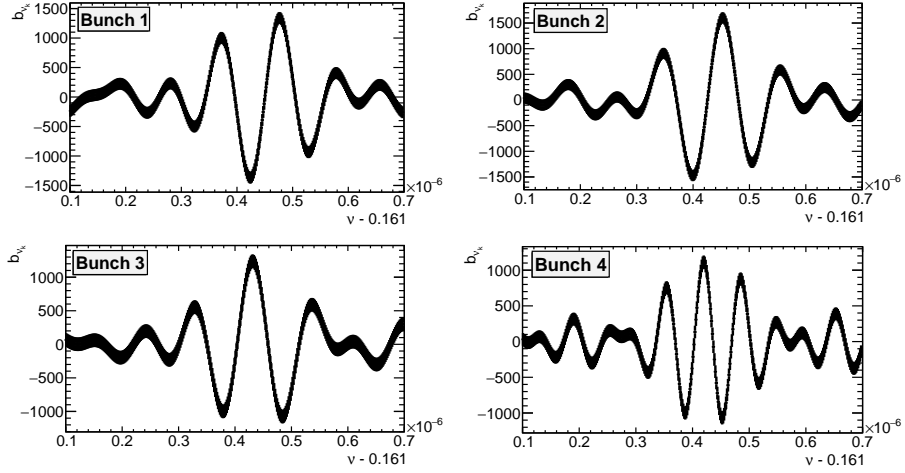


Figure 4.2: The number of events recorded versus the phase of the COSY RF-cavity showing the four separate bunches. Each recorded event records the rf-phase, along with turn number, polarization state and other variables, which can then be used while analyzing bunches separately.

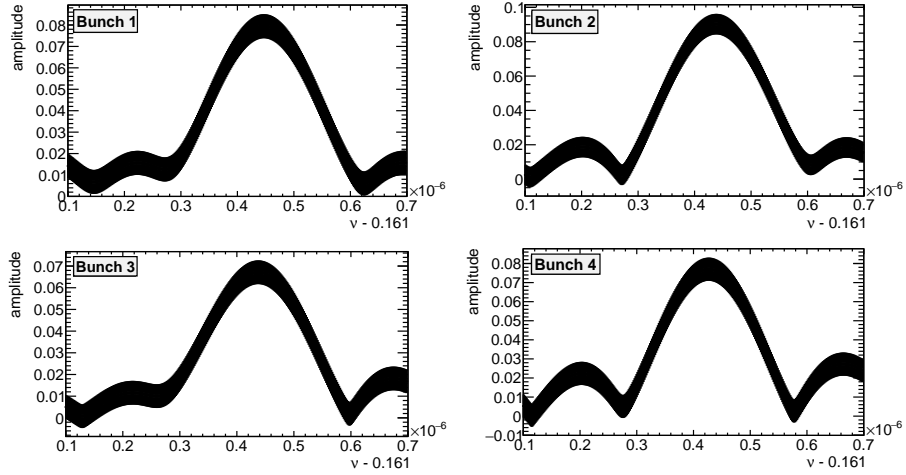
In COSY, we look at the phase of the COSY-RF cavity (Fig. 4.2). Here, we can see the four bunches separated in the space of rf-phase. In this chapter, the results of the analysis described in chapter 3 are presented for the separate bunches.

## 4.1 Results from the Analysis

The Fourier analysis procedure described in the previous section, along with the results given, were for one particle bunch in the cycle. Here we will compare the results between the bunches. In order to distinguish between the bunches, the phase of the COSY rf-cavity is used (Fig. 4.2). In Fig. 4.3a, the Fourier coefficient  $b_{\nu_k}$ , calculated during the discrete turn Fourier transform using Eq. 3.15, is shown for the first turn bin in four bunches. Fig. 4.3b shows the Fourier amplitudes in the four bunches, calculated using Eq. 3.17. The phase of the Fourier transforms are calculated, using Eq. 3.18, and plotted, and then fitted with a second order polynomial Eq. 3.27, Fig. 4.4a. Using this, the turn dependent spin tune can be plotted, Eq. 3.29, Fig. 4.4b. The spin tune shows a similar behaviour in all four of the bunches, although the absolute values differ from turn to turn. The consistency of these results are verified in the next section. Along with the turn dependent spin tune, we also plot the uncertainty of the spin tune, Eq. 3.55. Fig. 4.5 shows that the minimum uncertainty in the spin tune in all four bunches is of the order of  $10^{-11}$ .

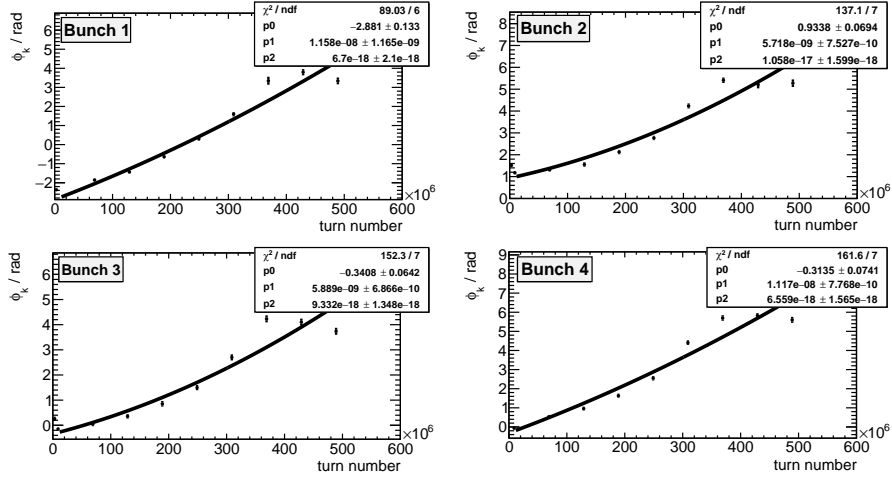


(a) The Fourier coefficient  $b_{\nu_k}$  at the first turn bin for the four bunches in the up detector.

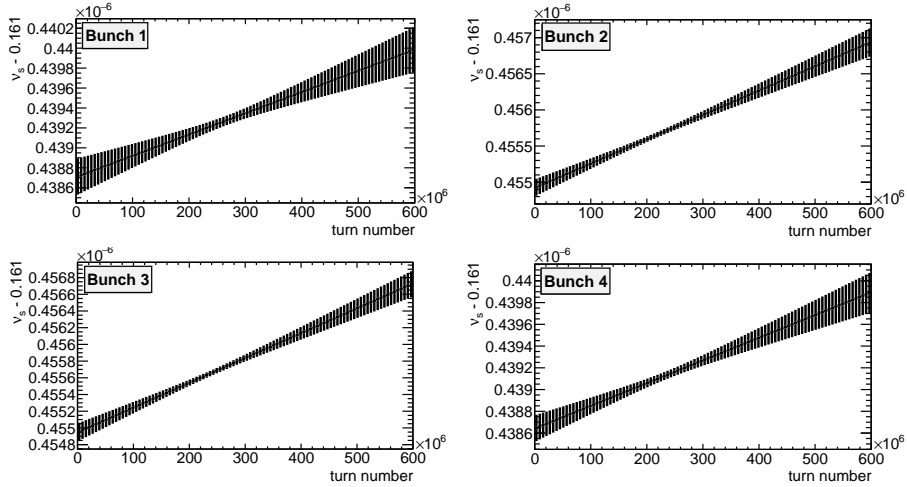


(b) The Fourier amplitude calculated at the first turn bin in the four bunches for the down detector.

Figure 4.3: Fourier spectrum and amplitude for the four bunches. When the phase for the Fourier spectrum is calculated, the frequency range is formed by taking the frequency of the maxima in the amplitude plots. Then for each frequency, each plot of the Fourier coefficients is scanned and the coefficient at that particular frequency is used.



(a) The phase calculated in the up detector at certain fixed frequencies in the four bunches.



(b) The turn dependent spin tune in the four bunches in the up detector.

Figure 4.4: Each phase plot is calculated using a different fixed spin tune frequency and then a second order polynomial is fitted onto the plot. The turn dependent spin tune is obtained using this fit and the fixed spin tune for the phase plot.

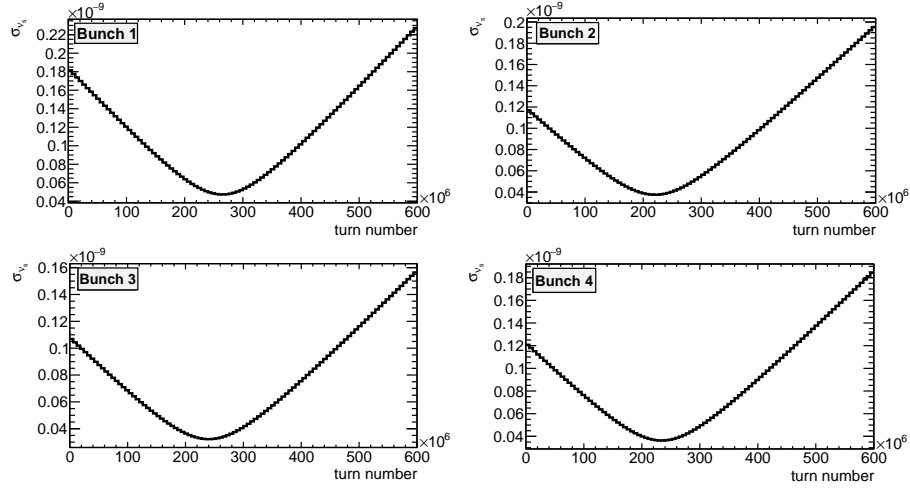
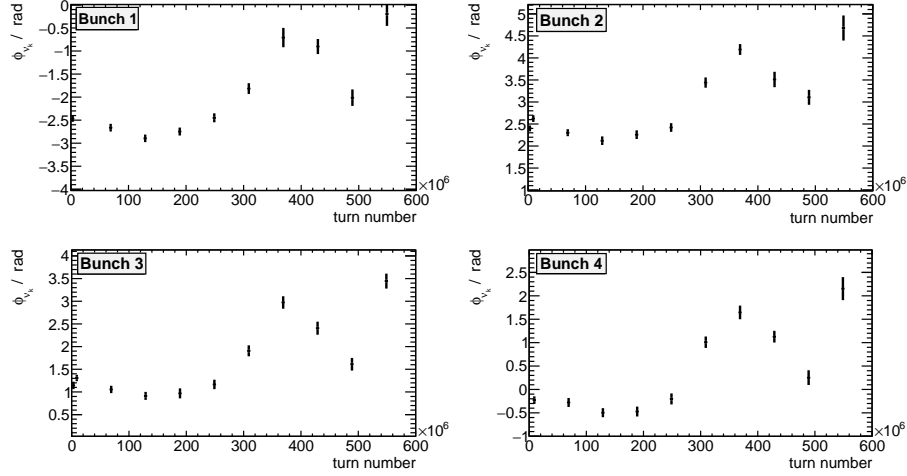


Figure 4.5: The uncertainty in the spin tune in the four bunches in the up detector. The minimum uncertainty in all four bunches is of the order of  $10^{-11}$ .

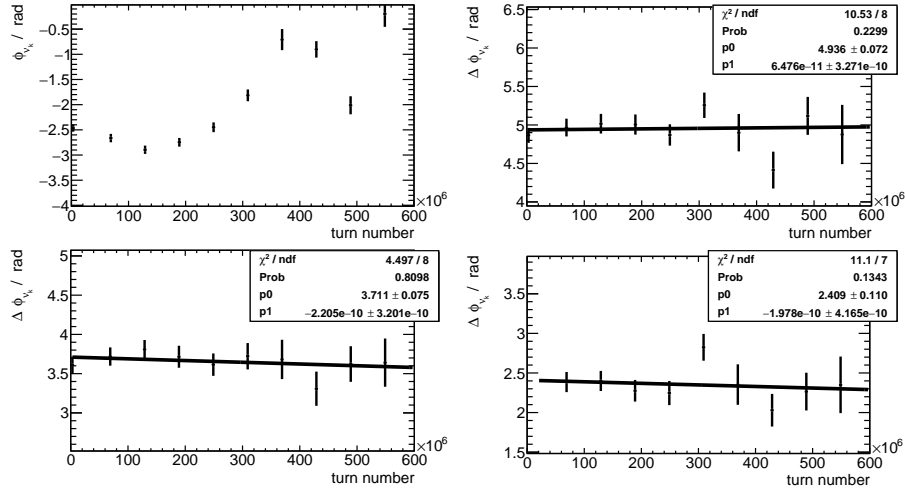
## 4.2 Consistency Check

As seen in Fig. 4.4b, the values of the spin tune in each bunch differs, even though the general behaviour is similar. In order to verify the consistency of the analysis being performed, the phases of the Fourier transform are compared between the bunches.

The Fourier spectrum, i.e. the coefficients defined in Eq. 3.15, is obtained by scanning all the events and performing the discrete transformation. In order to facilitate an efficient and manageable data set to handle, the cycle is divided into macroscopic turn (equivalently time) bins. Therefore, each plot is of one macroscopic turn bin showing the Fourier coefficient, either  $a_{\nu_k}$  or  $b_{\nu_k}$ , versus the frequency range, which can be changed depending on how finely we want to analyze the frequency decomposition. In order to calculate and plot the phase of the Fourier transform, a frequency range is formed by taking the frequency at which the Fourier amplitude reaches its maximum and adding equal intervals before and after it. Now the frequency range is scanned, and for each frequency the Fourier spectrum is scanned, taking the coefficients from each turn bin and calculating the phase, according to Eq. 3.18. The phase plots for a fixed frequency  $\nu = 0.161\,000\,439$  for the four bunches can be seen in Fig. 4.6a. Once the phases are obtained, for each bunch separately, taking one bunch as a reference, the phases of the other three bunches are subtracted from the reference, Fig. 4.6b. The difference between the phases of the bunches must remain constant. Therefore, if a straight line is fitted to the plots where the phases have been subtracted from the reference, its slope must be consistent with zero, within measurement errors.



(a) Phase calculated at the same fixed frequency  $\nu = 0.161\,000\,439$  in all four bunches. The first bunch is used as the reference.



(b) The phases of the second, third and fourth bunches are subtracted from the first bunch. A straight line is then fitted to the result. The fit parameters  $p0$  and  $p1$  correspond to the intercept and slope of the straight line, respectively.

Figure 4.6: The phases in the four bunches for a particular fixed frequency (a), and the difference from the reference and fit with a straight line (b).

# Chapter 5

## Summary

In order to measure the EDM of particles, which is the goal of the JEDI Collaboration, one of the quantities which is of great importance is the spin tune. A long spin coherence time is required to make accurate measurements of the EDM. The experiment is performed at COSY, a magnetic storage ring in Forschungszentrum Jülich. A deuteron beam which is spin polarized is injected into the ring and accelerated to 970 MeV/c. Due to the magnetic field, the spin starts to precess around the polarization axis, the motion being defined by the Thomas-BMT equation. The spin tune is the number of times the spin vectors precess about their axis per particle turn in the storage ring.

The run from April 2019, number 51180, was analyzed in this thesis. The run consisted of 4 cycles, 2 of which were polarized, cycles 1 and 3. The results of the analysis of the first cycle have been presented, and the results of the third cycle are in the appendix A. The beam was bunched into four bunches, and each bunch was analyzed separately. The Fourier method was used for the analysis and the turn dependent spin tune was determined for each bunch. The cycle length was of the order of  $10^3$  seconds and the beam was extracted in ten measurement intervals distributed over the cycle. The uncertainty in the spin tune, which is inversely related to the length of the cycle, is seen to be in the order of  $10^{-11}$  for all the bunches, and this result fits well with previous results where cycles of length  $10^2$  seconds had an uncertainty of the order of  $10^{-10}$  [16].

The spin tune from the four bunches was expected to behave the same. The behaviour is, evidently, similar for all four quantities, however we see a similarity in absolute magnitude of the spin tunes for the first and third bunches, and for the second and fourth bunches, respectively. In order to check the consistency of these results, the phase of the Fourier spectra for the separate bunches was analyzed. By taking the first bunch as a reference at a fixed frequency, the phase was plotted, and the phase from the other three bunches at the same frequency was compared to the first. By taking a difference and then fitting a straight line, we see that the slope of the fit is zero, within measurement errors, i.e. the difference in phase between the first bunch and the other three bunches remain constant, indicating a consistent set of measurements.

# Appendix A

## Results from Cycle 3

The results from the analysis for the third cycle are presented in this appendix. The Fourier spectrum, amplitude, phase, spin tune, and uncertainty in the spin tune is presented in the following figures. The uncertainty in the spin tune is also of the order of  $10^{-11}$ , as is the case in the first cycle. The consistency is checked and the results are found to show no significant differences between the bunches.

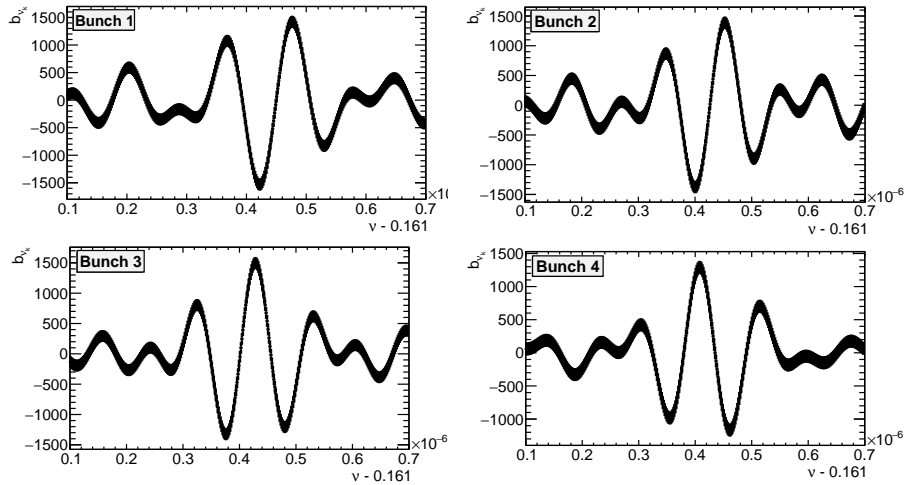


Figure A.1: The fourier coefficient  $b_{\nu_k}$  for the up detector in the first macroscopic time bin in the four bunches in cycle 3. Note the  $x$ -axis offset.

APPENDIX A. RESULTS FROM CYCLE 3

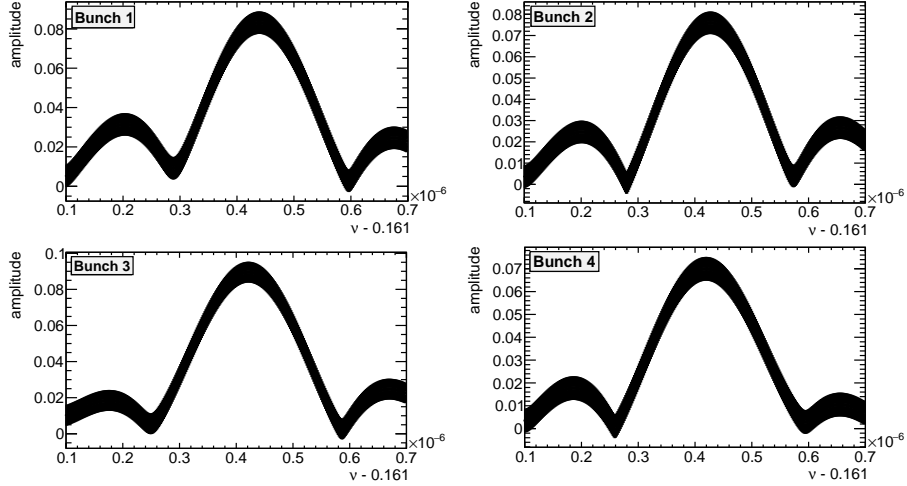


Figure A.2: The Fourier amplitude calculated for the up detector in the four bunches in cycle 3.

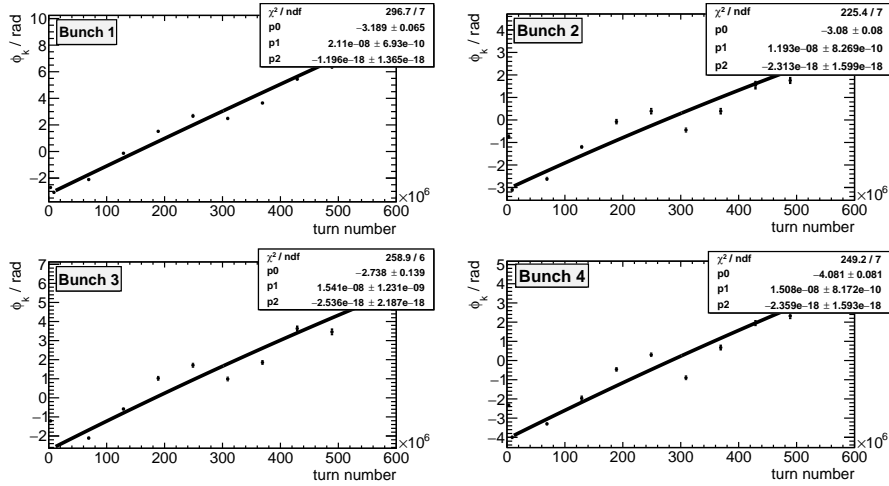


Figure A.3: The phase of the Fourier spectrum in the up detector for the four bunches in cycle 3, fitted with a second order polynomial. The subscript of fit parameters correspond to the respective powers of the turn number in the fit function.

APPENDIX A. RESULTS FROM CYCLE 3

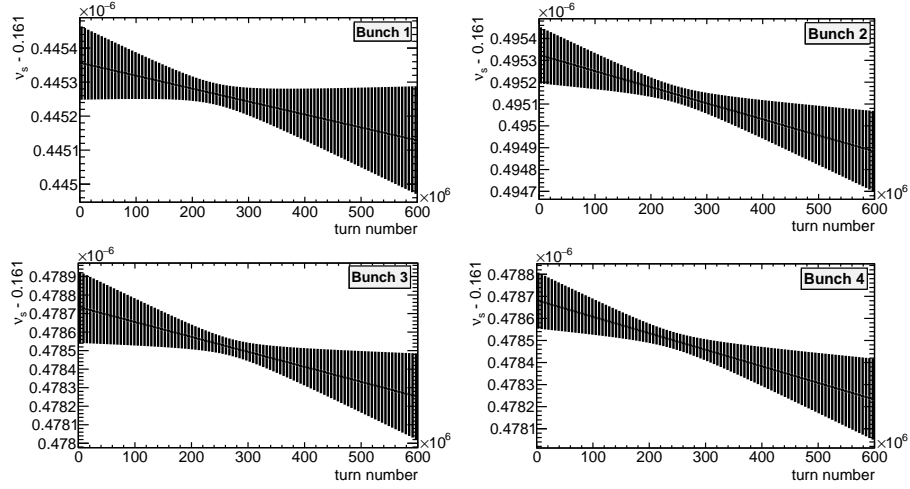


Figure A.4: The turn dependent spin tune in the four bunches of cycle 3. Note the  $y$ -axis offset.

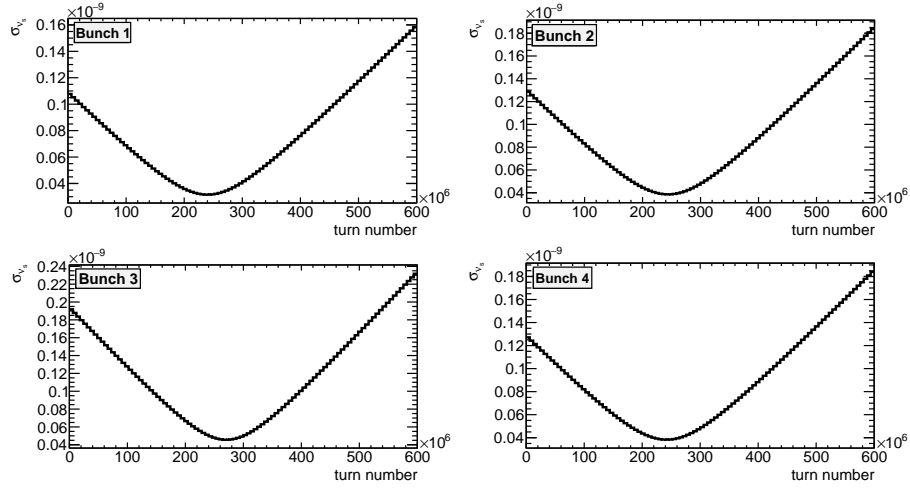


Figure A.5: Uncertainty in the spin tune for the four bunches in cycle 3

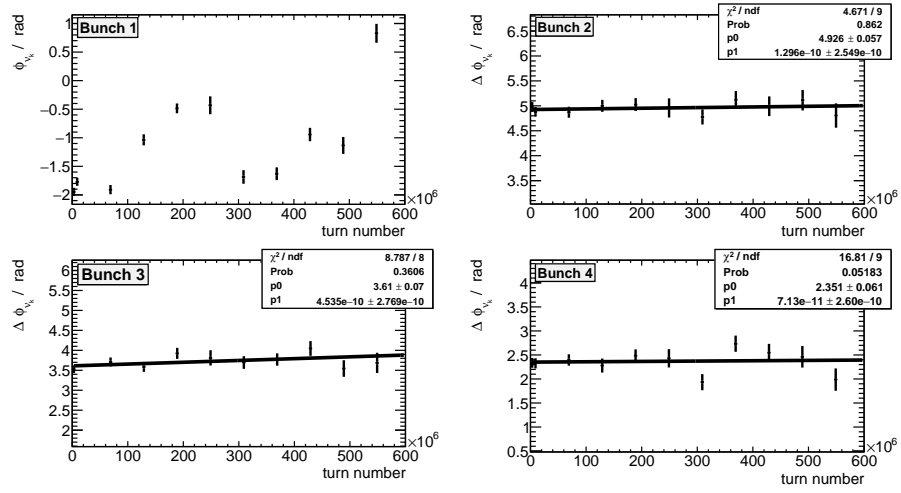


Figure A.6: Using the same method described in chapter 4.2, the results for cycle 3 are checked for their consistency. Plotting the phase at a fixed frequency for the four bunches, the difference between bunch 1 and the other three is plotted and fitted with a straight line. The difference should remain constant and the slope of the fit should be consistent with zero. This can be seen from the plots. Here, the phase was plotted at the fixed frequency of  $\nu_s^0 = 0.161\,000\,428$ .

# Bibliography

- [1] A.D. Sakharov. “Violation of CP Invariance, C asymmetry, and baryon asymmetry of the universe”. In: *Sov. Phys. Usp.* 34.5 (1991), pp. 392–393. DOI: 10.1070/PU1991v034n05ABEH002497.
- [2] Planck Collaboration. “Planck 2018 results. VI. Cosmological parameters”. In: (2018), p. 70. arXiv: 1807.06209 [astro-ph.CO].
- [3] Mayumi Aoki, Akio Sugamoto, and Noriyuki Oshimo. “Implications of baryon asymmetry for the electric dipole moment of the neutron”. In: *Prog. Theor. Phys.* 98 (1997), pp. 1325–1332. DOI: 10.1143/PTP.98.1325. arXiv: hep-ph/9706287.
- [4] Laurent Canetti, Marco Drewes, and Mikhail Shaposhnikov. “Matter and antimatter in the universe”. In: *New Journal of Physics* 14.9 (Sept. 2012), p. 095012. ISSN: 1367-2630. DOI: 10.1088/1367-2630/14/9/095012. URL: <http://dx.doi.org/10.1088/1367-2630/14/9/095012>.
- [5] Latham Boyle, Kieran Finn, and Neil Turok. “CPT-Symmetric Universe”. In: *Phys. Rev. Lett.* 121 (25 Dec. 2018), p. 251301. DOI: 10.1103/PhysRevLett.121.251301. URL: <https://link.aps.org/doi/10.1103/PhysRevLett.121.251301>.
- [6] Christopher T. Hill. “Axion induced oscillating electric dipole moment of the electron”. In: *Physical Review D* 93.2 (Jan. 2016). ISSN: 2470-0029. DOI: 10.1103/physrevd.93.025007. URL: <http://dx.doi.org/10.1103/PhysRevD.93.025007>.
- [7] Yuichiro Nakai and Matthew Reece. “Electric dipole moments in natural supersymmetry”. In: *Journal of High Energy Physics* 2017.8 (Aug. 2017). ISSN: 1029-8479. DOI: 10.1007/jhep08(2017)031. URL: [http://dx.doi.org/10.1007/JHEP08\(2017\)031](http://dx.doi.org/10.1007/JHEP08(2017)031).
- [8] JEDI Collaboration. URL: <http://collaborations.fz-juelich.de/ikp/jedi/>.
- [9] J. H. Christenson et al. “Evidence for the  $2\pi$  Decay of the  $K_2^0$  Meson”. In: *Phys. Rev. Lett.* 13 (4 July 1964), pp. 138–140. DOI: 10.1103/PhysRevLett.13.138. URL: <https://link.aps.org/doi/10.1103/PhysRevLett.13.138>.

## BIBLIOGRAPHY

---

- [10] R. Aaij et al. “First Observation of CP Violation in the Decays of  $B_s^0$  Mesons”. In: *Physical Review Letters* 110.22 (May 2013). ISSN: 1079-7114. DOI: 10.1103/physrevlett.110.221601. URL: <http://dx.doi.org/10.1103/PhysRevLett.110.221601>.
- [11] G. 't Hooft. “Symmetry Breaking through Bell-Jackiw Anomalies”. In: *Phys. Rev. Lett.* 37 (1 July 1976), pp. 8–11. DOI: 10.1103/PhysRevLett.37.8. URL: <https://link.aps.org/doi/10.1103/PhysRevLett.37.8>.
- [12] Maxim Pospelov and Adam Ritz. “Electric dipole moments as probes of new physics”. In: *Annals of Physics* 318.1 (July 2005), pp. 119–169. ISSN: 0003-4916. DOI: 10.1016/j.aop.2005.04.002. URL: <http://dx.doi.org/10.1016/j.aop.2005.04.002>.
- [13] C. Abel et al. “Measurement of the Permanent Electric Dipole Moment of the Neutron”. In: *Phys. Rev. Lett.* 124 (8 Feb. 2020), p. 081803. DOI: 10.1103/PhysRevLett.124.081803. URL: <https://link.aps.org/doi/10.1103/PhysRevLett.124.081803>.
- [14] W. C. Griffith et al. “Improved Limit on the Permanent Electric Dipole Moment of  $^{199}\text{Hg}$ ”. In: *Phys. Rev. Lett.* 102 (10 Mar. 2009), p. 101601. DOI: 10.1103/PhysRevLett.102.101601. URL: <https://link.aps.org/doi/10.1103/PhysRevLett.102.101601>.
- [15] H. Stein et al. “Current Status of the COSY Electron Cooler (Jülich, Germany)”. In: *Atomic Energy* 94 (Jan. 2003), pp. 24–26. DOI: 10.1023/A:1023486402224.
- [16] G. Guidoboni et al. “How to Reach a Thousand-Second in-Plane Polarization Lifetime with 0.97–GeV/c Deuterons in a Storage Ring”. In: *Phys. Rev. Lett.* 117 (5 July 2016), p. 054801. DOI: 10.1103/PhysRevLett.117.054801. URL: <https://link.aps.org/doi/10.1103/PhysRevLett.117.054801>.
- [17] J. J. Sakurai and Jim Napolitano. *Modern Quantum Mechanics*. 2nd ed. Cambridge University Press, 2017. DOI: 10.1017/9781108499996.
- [18] Denis Eversmann. “High Precision Spin Tune Determination at the Cooler Synchrotron in Jülich - PhD thesis”. In: (Oct. 2018). URL: [http://collaborations.fz-juelich.de/ikp/jedi/public\\_files/theses/ThesisEversmann\\_v1.pdf](http://collaborations.fz-juelich.de/ikp/jedi/public_files/theses/ThesisEversmann_v1.pdf).
- [19] L.H. Thomas B.A. “I. The kinematics of an electron with an axis”. In: *The London, Edinburgh, and Dublin Philosophical Magazine and Journal of Science* 3.13 (1927), pp. 1–22. DOI: 10.1080/14786440108564170. eprint: <https://doi.org/10.1080/14786440108564170>. URL: <https://doi.org/10.1080/14786440108564170>.
- [20] Gerald G. Ohlsen and P.W. Keaton. “Techniques for measurement of spin-1/2 and spin-1 polarization analyzing tensors”. In: *Nuclear Instruments and Methods* 109.1 (1973), pp. 41–59. ISSN: 0029-554X. DOI: [https://doi.org/10.1016/0029-554X\(73\)90450-3](https://doi.org/10.1016/0029-554X(73)90450-3). URL: <http://www.sciencedirect.com/science/article/pii/0029554X73904503>.

## BIBLIOGRAPHY

---

- [21] Fabian Müller. “Polarimeter Development for Electric Dipole Moment Measurements in Storage Rings”. RWTH Aachen, Nov. 2019, p. 28. URL: [http://collaborations.fz-juelich.de/ikp/jedi/public\\_files/theses/thesis\\_fabian\\_mueller\\_final\\_version.pdf](http://collaborations.fz-juelich.de/ikp/jedi/public_files/theses/thesis_fabian_mueller_final_version.pdf).
- [22] Marilène Da Silva E Silva. “Sensitive polarimetry in a search for the deuteron electric dipole moment”. English. Relation: <https://www.rug.nl/Rights>: University of Groningen. PhD thesis. University of Groningen, Feb. 2010. ISBN: 9789036742740.
- [23] D. Prasuhn et al. “Electron and stochastic cooling at COSY”. In: *Nuclear Instruments and Methods in Physics Research Section A: Accelerators, Spectrometers, Detectors and Associated Equipment* 441 (Feb. 2000), pp. 167–174. DOI: 10.1016/S0168-9002(99)01128-6.
- [24] Z. Bagdasarian et al. “Measuring the polarization of a rapidly precessing deuteron beam”. In: *Phys. Rev. ST Accel. Beams* 17 (5 May 2014), p. 052803. DOI: 10.1103/PhysRevSTAB.17.052803. URL: <https://link.aps.org/doi/10.1103/PhysRevSTAB.17.052803>.
- [25] Marcel Rosenthal. “Experimental Benchmarking of Spin Tracking Algorithms for Electric Dipole Moment Searches at the Cooler Synchrotron COSY - Ph.D. Thesis”. In: (May 2016). URL: [http://collaborations.fz-juelich.de/ikp/jedi/public\\_files/theses/Thesis\\_MRosenthal.pdf](http://collaborations.fz-juelich.de/ikp/jedi/public_files/theses/Thesis_MRosenthal.pdf).
- [26] Denis Eversmann. “Analysis of the Spin Coherence Time at the Cooler Synchrotron COSY - Master’s thesis”. In: (Mar. 2013). URL: [http://collaborations.fz-juelich.de/ikp/jedi/public\\_files/theses/DEMsterarbeit.pdf](http://collaborations.fz-juelich.de/ikp/jedi/public_files/theses/DEMsterarbeit.pdf).
- [27] K. F. Riley, M. P. Hobson, and S. J. Bence. *Mathematical Methods for Physics and Engineering*. Cambridge University Press, 2006, pp. 433–435.
- [28] Jörg Pretz. “Statistical Uncertainties of Frequency Measurements - JEDI Internal Note”. In: (Apr. 2014). URL: [http://collaborations.fz-juelich.de/ikp/jedi/private\\_files/intnotes/freq\\_measurement.pdf](http://collaborations.fz-juelich.de/ikp/jedi/private_files/intnotes/freq_measurement.pdf).
- [29] Roger Barlow. *Statistics - A Guide to the Use of Statistical Methods in the Physical Sciences*. John Wiley and Sons Ltd., 1999, pp. 103–104.
- [30] D. Eversmann et al. “New Method for a Continuous Determination of the Spin Tune in Storage Rings and Implications for Precision Experiments”. In: *Phys. Rev. Lett.* 115 (9 Aug. 2015), p. 094801. DOI: 10.1103/PhysRevLett.115.094801. URL: <https://link.aps.org/doi/10.1103/PhysRevLett.115.094801>.
- [31] Helmut Wiedemann. *Particle Accelerator Physics*. 3rd ed. Springer-Verlag Berlin Heidelberg, pp. 541–543. DOI: 10.1007/978-3-540-49045-6.

# List of Figures

1.1	EDM and its transformations . . . . .	2
1.2	COSY outline . . . . .	4
2.1	Coordinate system used in the experiment . . . . .	9
2.2	WASA polarimeter . . . . .	10
3.1	Number of events recorded throughout the cycle . . . . .	12
3.2	Visual representation of the regular Fourier transform . . . . .	14
3.3	Number of events in the four detector quadrants . . . . .	18
3.4	Fourier spectrum in different frequency ranges . . . . .	18
3.5	Amplitude of Fourier transform . . . . .	19
3.6	Amplitude and Phase . . . . .	19
3.7	Phase in the up and down detectors at different frequencies . . . . .	22
3.8	Phase of Fourier transform fitted with a second order polynomial . . . . .	23
3.9	Spin tune versus turn number for the up and down detectors . . . . .	23
3.10	Spin tune uncertainty in up and down detectors . . . . .	24
4.1	Principle of particle bunching in beams . . . . .	28
4.2	COSY RF-phase . . . . .	29
4.3	Fourier spectrum and amplitude of the four bunches . . . . .	30
4.4	Phase and turn dependent spin tune in the four bunches . . . . .	31
4.5	Uncertainty in the spin tune in four bunches . . . . .	32
4.6	Phase and difference between phases between bunches . . . . .	33
A.1	Fourier spectrum in the up detector in cycle 3 . . . . .	35
A.2	Fourier amplitude in the up detector in cycle 3 . . . . .	36
A.3	Phase of the Fourier spectrum in the up detector for four bunches in cycle 3 . . . . .	36
A.4	Spin tune in the up detector for the four bunches in cycle 3 . . . . .	37
A.5	Uncertainty in the spin tune for the four bunches in cycle 3 . . . . .	37
A.6	Consistency check for the four bunches in cycle 3 . . . . .	38



# Acknowledgements

I would like to thank Prof. Pretz for giving me the opportunity to work in the JEDI Collaboration and for his continued guidance. The atmosphere and work environment fostered in the group made working an enjoyable and educational experience.

I would also like to thank Prof. Stahl for accepting to be my second supervisor for my thesis, and for the support and advice he offers to international students, and to Dr. Hejny for his guidance during the analysis.

Thank you to all the members of JEDI and IKP, especially Achim, Vera, Max, Christian, Saad, and Benat, for delicious cakes on Wednesdays and for innumerable discussions over coffee.

Finally, I would like to thank my family, my parents and sister, without whom I would not be where I am today. Their unconditional support was a vital part of my work and this thesis would not have been possible without it.